Version of Record: https://www.sciencedirect.com/science/article/pii/S1359431121002325
Manuscript_74b4b985046cee324356efc2b0641ed5

Effect of Non-Condensable Gas on Heat Transfer within the Hollow Fin Condenser of Metallic and Polymer Vapor Chambers

Elise Bérut, Stéphane Lips, Frédéric Lefèvre, Valérie Sartre*
Univ Lyon, CNRS, INSA-LYON, CETHIL UMR5008, F-69621 Villeurbanne, France

*Corresponding author. E-mail address: valerie.sartre@insa-lyon.fr (V. Sartre)

Abstract

A vapor chamber with hollow fins was manufactured and tested with condensers made of polymer and aluminum. The fins are 5.3 mm in inner diameter and cooled by forced air convection. The use of polymer instead of aluminum has little influence on the performance: it is of interest for weight reduction when the cooling medium is air. The impact of non-condensable gas (NCG) is studied experimentally using IR temperature measurements on the fins and performance monitoring over time. To complete the study, a numerical model of film condensation inside a vertical tube in the presence of NCG is developed. The model combines hydrodynamic and axial mass diffusion phenomena with 2D heat conduction in the wall. A good agreement is found between experimental results and model predictions. The effect of the NCG mass, heat load, external cooling coefficient and wall thermal conductivity is studied though a parametric analysis. When the wall thermal conductivity increases, so does the volume occupied by NCG inside the fins and the performance degradation. In other words, aluminum condensers are more sensitive to NCG than polymer ones, and the difference is all the more important as external cooling is efficient.

Keywords: condensation, non-condensable gas, vapor chamber, hollow fins, polymer

Introduction

With the decrease in the size of electronic components leading to ever-increasing heat flux levels, thermal management has become a major concern in the electronic industry. Heat pipes and vapor chambers have proven to be amongst the most efficient passive cooling devices, but the research is ongoing to improve the design of these systems. Traditionally, vapor chambers are used as heat spreaders and associated with solid air-cooled finned heat sinks. The heat sink is then placed directly above the condensation zone. For this study however, a thermosyphon vapor chamber with integrated hollow fins was built and tested. This condenser design has the following benefits: no contact thermal resistance between the vapor chamber and the finned region and high fin efficiency. Thanks to the fluid condensation inside the fins, they are indeed virtually isothermal, resulting in better thermal performance compared to traditional air-cooled heat sinks.

In addition, the condenser is made of polymer: it is a lightweight and cheap material allowing great design liberty thanks, in particular, to recent progress in additive manufacturing. Polymer materials are of interest for applications requiring weight reduction such as transportation systems, especially when the cooling medium is air. However, polymers also have challenging properties in relation to heat pipes, such as low thermal conductivity and barrier properties. In air-cooled polymer heat pipes, condenser wall thermal resistance can be negligible when compared to convective thermal resistance if the wall is thin. When designing the system, one must find the best compromise between wall thermal and mechanical resistances. The wall thickness also affects the permeability of the casing, which is of critical importance in heat pipes. Low barrier properties of polymers associated

with thin walls may cause non-condensable gas (NCG) to enter the system when under negative pressure and reduce its performance [1-2]. The presence of NCG might also result from a chemical reaction of the working fluid and case material, from degassing of inner surfaces or of the working fluid itself if not properly degassed. Therefore, the prediction of the impact of NCG on heat pipes performance over time is required to evaluate the average lifespan of these systems.

Many researchers have studied the impact of NCG on heat pipes behavior and performance through modelling and, to a lesser extent, experiments. The models of gas-loaded heat pipes were first developed in the 1970s for the design of variable conductance heat pipes (VCHP). Gas-loaded heat pipe models present different levels of complexity in the treatment of mass diffusion between vapor and NCG, from simple flat-front models to sophisticated two-dimensional models, usually solved using numerical methods. Flat-front models, such as Marcus and Fleischman's [3] (steady state) or Faghri and Harley's [4] (transient), involve many approximations but they are widely used because they provide a convenient and sufficiently accurate tool for heat pipe design, especially when they include axial conduction in the pipe wall. They are based on the assumption that NCG forms a gas plug at the condenser end, acting as a diffusion barrier to the flowing vapor, and that a sharp interface exists between the vapor and NCG-blocked portions of the condenser.

One-dimensional diffusion models are physically more realistic than flat-front models because they include the effect of axial mass diffusion on the vapor-gas interface through Fick's law of binary diffusion, but they usually require an iterative resolution. Several authors developed 1D models for capillary heat pipes [5-8], in which an equivalent thermal conductivity of the liquid-filled wick is estimated. For thermosyphons, on the other hand, the condensate film thickness must be known at every axial position to evaluate the induced additional thermal resistance. Consequently, capillary heat pipe models are not directly applicable to thermosyphons. In the literature, thermosyphon models are mostly two-dimensional, accounting for both axial and radial mass diffusion in the vapor-gas interface.

Two-dimensional models are the most rigorous and accurate, but they are computationally time consuming. Rohani and Tien [9] and Harley and Faghri [10] developed a 2D model of gas-loaded capillary heat pipe in steady and transient conditions, respectively. Concerning 2D diffusion models for thermosyphons, many studies are based on the work of Hijikata *et al.* [11] such as Peterson and Tien's [12] or Zhou and Collins' [13]. Hijikata's physical model deals with condensation of pure saturated vapor flowing vertically upward from the evaporator, as shown schematically in Fig. 1. In the figure, the interface of NCG and vapor is a parabolic-shaped region. Radial mass diffusion is indeed considered and causes NCG to accumulate at the vapor-liquid interface. In 1994, Harley and Faghri [14] also presented a transient two-dimensional model for gas-loaded thermosyphons, which includes the falling condensate film and the conjugate heat transfer through the wall.

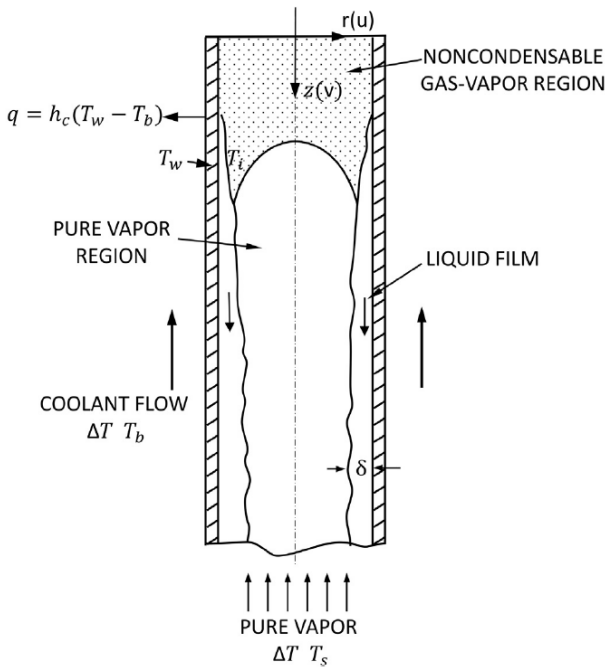

Fig. 1. Schematic of the condenser in a two-phase closed thermosyphon [11]

Previous studies indicate that a small amount of NCG can have a great inhibitory effect on condensation and, therefore, considerably deteriorate the performance of heat pipes. When the NCG mass increases at constant heat input, the active condenser section is reduced, resulting in a higher operating temperature. It was determined that this phenomenon is nonlinear in nature [14]. Besides, it has been shown that axial conduction in the pipe wall strongly influences the predicted position of the vapor-gas interface and the temperature profiles [3-5,14]. Research on VCHPs for space applications [15-17] or vehicle thermal management [18] is ongoing. The latest studies largely focus on loop heat pipes (LHP) [19-25] and few have been recently published concerning thermosyphons. In 2018, Kim *et al.* [26] experimentally studied the effect of NCG on heat transfer in a thermosyphon by varying its inclination angle while, in 2020, Yuan *et al.* [27] developed a CFD simulation to analyze the performance of their gas-loaded thermosyphon.

It should be noted that metallic heat pipes were considered in the vast majority of the previous works, with the exception of Peterson and Tien's. The latter have indeed tested a water-cooled glass thermosyphon containing NCG [28] and extended their model to low thermal conductance walls with low condenser external heat transfer coefficients [12]. However, Peterson and Tien's model does not include radial heat conduction through the wall and condensate film and it can only be used in cases where heat conduction in the wall is either dominant or negligible [29]. Some authors conducted tests with low external coefficients [5,9], but these were never associated with a low thermal conductance wall to our knowledge.

To fill this gap, the present study investigates both experimentally and theoretically the impact of NCG in an air-cooled polymer condenser vapor chamber: its originality lies in the combination of a low thermal conductance wall with a low condenser external heat transfer coefficient (about 100 W/m².K). An aluminum condenser of same geometry was also manufactured and tested for comparison. The aim is to study the influence of the wall thermal conductance, the external cooling conditions and other parameters on the hollow fins' temperature in the presence of NCG and on the vapor chamber's performance. This paper includes three parts. The first part is dedicated to the presentation of the experimental bench and some experimental results obtained using the mentioned air-cooled polymer condenser, as well as an aluminum condenser of same geometry. The second part describes the numerical model with its assumptions. In the last part, model predictions are compared with experimental results and a parametric study is conducted and discussed.

1. Experimental study of a vapor chamber with hollow fins in the presence of non-condensable gas

1.1 Experimental setup

The vapor chamber under investigation, shown in Fig. 2, has a flat circular geometry. It is made of two parts: a polymer condenser and a copper evaporator casing, which are clamped together with a 156 mm inner diameter seal between them to form a vacuum tight vapor space 13 mm high (Fig. 3). The vapor chamber works as a thermosyphon: the fluid circulation is driven by gravity, with the condenser above the evaporator. A range of small parallel grooves is engraved at the center of the evaporator casing inner wall to enhance nucleate boiling.

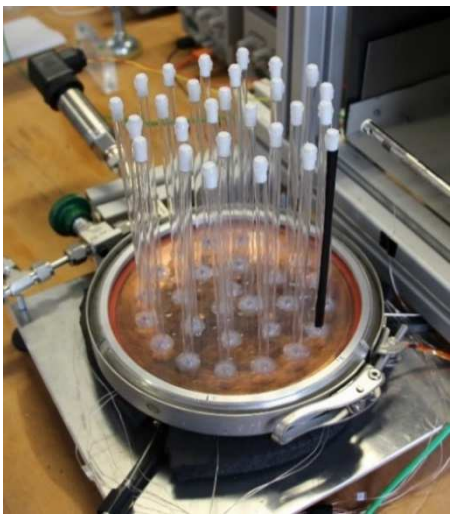

Fig. 2. Picture of the thermosyphon vapor chamber with transparent hollow fins

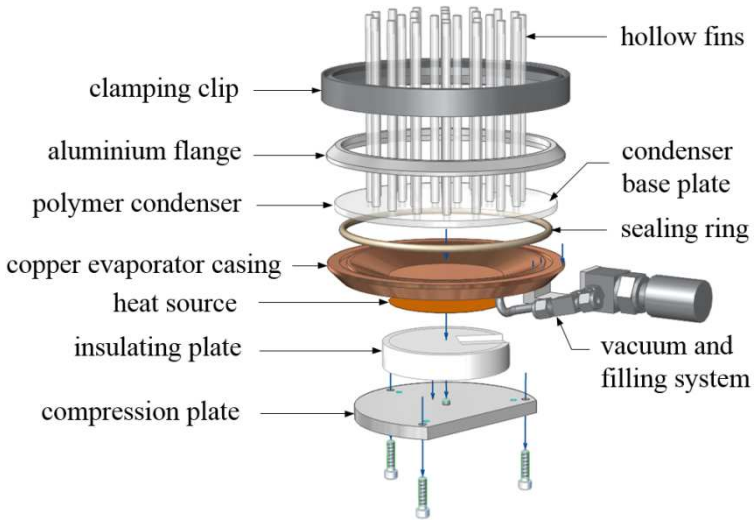

Fig. 3. Vapor chamber assembly (exploded view)

The condenser is made of 27 cylindrical hollow fins with inner diameter 5.3 mm glued to a 5 mm thick polycarbonate cover. The tubes are 14.5 cm high and made of polymer polyethylene terephthalate (PET). Each one is closed at its top by a 1 cm high PET plug, so the effective height for heat transfer is 13.5 cm. The thickness of the tubes wall, of 300 µm, is sufficient to withstand vacuum while minimizing the radial conductive thermal resistance of the wall. Besides being lightweight and cheap, the selected polymer materials are transparent, enabling visualization of hydrodynamic and phase change phenomena inside the device. An aluminum condenser was also manufactured by means of a laser powder bed fusion additive process in order to study the influence of the material on the vapor chamber performance. Its geometry is similar to the polymer condenser except for the wall thickness, which was increased to 1 mm, and the effective height, reduced to 10 cm because of additive manufacturing constraints.

The heat source is a resistive heater, 90 mm in diameter, supplying power up to 150 W (2.4 W/cm²). It is insulated and pressed against the evaporator casing by a compression plate, as seen in Fig. 3. The condenser is air cooled by fans placed in a steel duct. The air velocity is around 3.5 m/s and its temperature is maintained at 22.5 ± 1.5°C by means of an air-conditioner and warm air heating. The experimental setup is presented in Fig. 4.

Eleven K-type thermocouples made from 80 µm wire are located in grooves at the back of the evaporator casing. A thermocouple is also used to measure the air temperature, and an anemometer located at the outlet section of the air duct gives its velocity. The operating temperature T_{sat} of the vapor chamber is determined from the mean temperature of two mineral insulated thermocouples, 1.5 mm in diameter, placed inside the chamber. Besides, a Kistler pressure sensor located next to the filling valve measures the total working pressure. The power supplied by the heat source is measured

by means of a voltage divider coupled with a shunt resistor. Finally, visible and infrared visualizations are performed. The FLIR E6 infrared camera used to determine the tubes external temperature has a low accuracy but a thermal sensitivity smaller than 0.06°C, which is interesting to study the impact of NCG by means of temperature profiles along the fins.

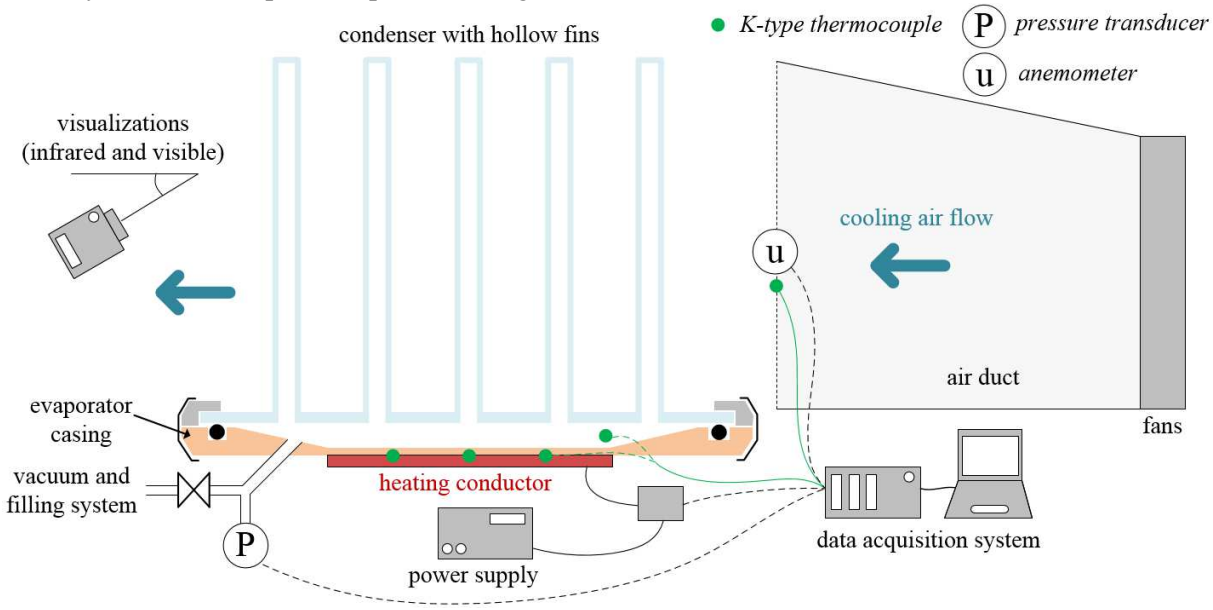

Fig. 4. Schematic of the experimental setup for thermal characterization

The vapor chamber is filled with n-pentane, previously degassed in a dedicated container. Pentane was selected because it is compatible with PET and polycarbonate and, unlike water, its wettability on polymer surfaces is high, promoting filmwise condensation inside the hollow fins. Besides, its physical and thermal properties are well known and its high saturation pressure is favorable when one wants to minimize leaks. Experiments were carried out varying the heat transfer rate and liquid fill charge. The latter parameter will not be studied because it turned out to have no significant influence on the phenomena and performance of condensation. The heat transfer rate ranged from 7 to 75 W, with a relative uncertainty between 2 and 7%.

Since the internal pressure is lower than the external one, NCG continuously leaks inside the vapor chamber. Thus, the parameter t_{vacuum} was defined, which corresponds to the elapsed time from the last vacuum pumping of the vapor chamber: the longer the time t_{vacuum}, the higher the NCG mass. The mass leak rate of the prototype was estimated to $3\,mg.day^{-1}.bar^{-1}$ from pressure measurements over time, with both polymer and aluminum condensers. This high leak rate has made the study of NCG possible. Naturally, leaks would be negligible for industrial systems in a real environment, partly because there would be no sealing ring. Ideally, one should design heat pipes and vapor chambers in one piece to avoid assemblies and leaks. The present design was chosen for the possibility to test several condenser's geometry with a single prototype.

1.2 Infrared measurements

As mentioned in section 1.1, an IR camera FLIR E6 is used to determine the external temperature profile along the fins at steady state. Fig. 5 shows an example of thermal image of the polymer condenser in operation. An adhesive tape of emissivity 0.95 ± 0.03 in the spectral range of the camera (7.5 to 13 µm) was placed on tube #3 (Fig. 5). The software ImageJ is used for post-processing of grayscale thermal images. For each experimental point, temperature profiles of three tubes (Fig. 5) along the x axis are plotted, such as those displayed in Fig. 6. The axial position x is defined with $x = 0$ at the top of the tube – excluding the end cap – and $x = H_{tot}$ at the bottom. Several regions can be identified from the temperature profiles: the cold zone, the front region and the NCG-free area. Fig. 6 illustrates them for tube #3. The NCG-free area, which can be enlarged or reduced depending on the

operating conditions, is available for effective vapor condensation: the heat transfer intensity is the highest in this region. The slight temperature decrease observed along the NCG-free zone is related to the cooling air temperature, which is not homogeneous and lower at the bottom of the duct and fins.

It appears from the comparison of temperature profiles with and without adhesive tape that the tape does not have a significant influence, even more so as the uncertainty on the temperature is large, as shown in Fig. 6. For this reason, the three profiles are considered as valid. For each tube, the external wall temperature averaged over the whole height, noted $T_{w,ext,mean}$, is calculated. The three obtained values are averaged again to account for spatial variability. The uncertainty in the final mean temperature, of 3.2 K, integrates the specifications of the IR camera, the reproducibility of measurements, uncertainty in emissivity and potential bias introduced while plotting or processing the curves.

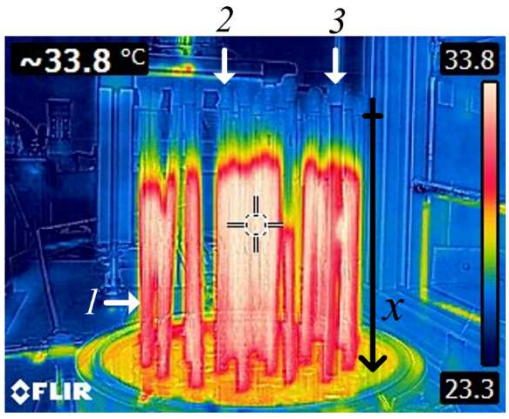

Fig. 5. Infrared image of the polymer condenser ($\dot{Q}_{tot} = 60\ W$, $t_{vacuum} = 3.5h$)

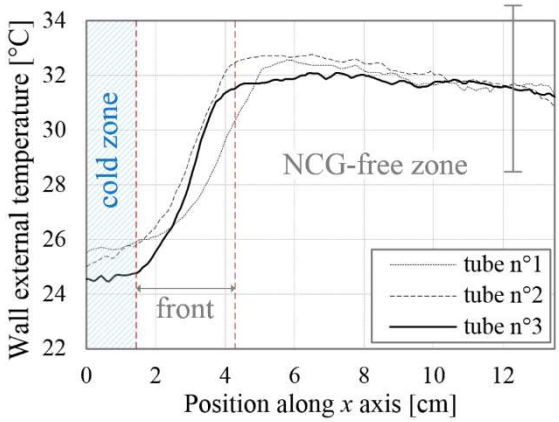

Fig. 6. Example of external wall temperature profiles (processed from Fig. 5)

The aluminum condenser was covered with a black paint of emissivity 0.92 ± 0.06 in the spectral range of the camera. Fig. 7 and 8 show an example of thermal image of the aluminum condenser and its associated wall temperature profiles. The curves are considerably different from those presented above. In the polymer case (Fig. 6), the temperature is stable in the lower part of the tubes and decreases steeply towards the air temperature at the top. For the aluminum condenser (Fig. 8), the external wall temperature decreases steadily along the fins, which makes it impossible to identify the position of a NCG zone. That is due to significant longitudinal heat conduction in aluminum, which tends to smooth the temperature profiles. The behavior of the NCG-loaded fins is therefore fairly affected by the conductivity of the wall material.

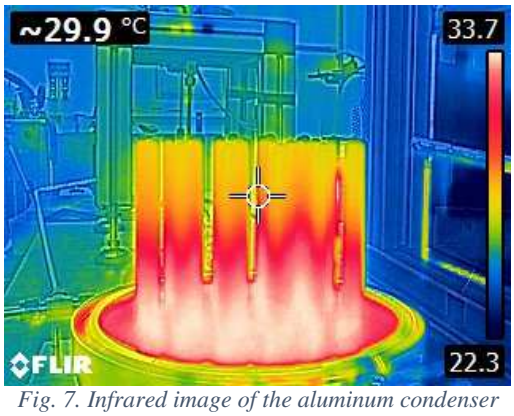

Fig. 7. Infrared image of the aluminum condenser ($\dot{Q}_{tot} = 60\ W$, $t_{vacuum} = 3h$)

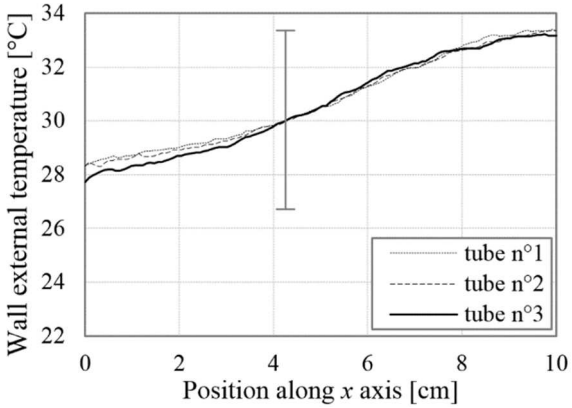

Fig. 8. Example of external wall temperature profiles (processed from Fig. 7)

1.3 Heat transfer data reduction

A simplified thermal model of the device using an equivalent electrical network is presented in Fig. 9. The global thermal resistance of the vapor chamber is defined using the mean temperature

difference between the evaporator and the cooling air at steady state and the total heat transfer rate $\dot{Q}_{tot}$:

$$R_{tot} = \frac{T_{evap,max} - T_{air}}{\dot{Q}_{tot}} \quad (1)$$

where $T_{evap,max}$ is the maximum temperature of the evaporator casing.

1.3.1 Heat load transferred by the fins

Part of the heat input is transferred by conduction through the casing, and then dissipated by convection and radiation to the ambient air. Most studies do not distinguish between phase change and conduction heat transfer but, in the present work, it is necessary to estimate the heat flux associated with conduction in the casing $\dot{Q}_{casing}$ in order to properly characterize the impact of the heat load on NCG distribution. Moreover, the heat load transferred by phase change at the evaporator $\dot{Q}_{pc}$ is also divided into two parts: $\dot{Q}_{base}$ is transferred by conduction through the condenser base plate and $\dot{Q}_{fins}$ is the heat effectively evacuated by the hollow fins. Only the latter must be considered for comparison with the numerical model results introduced in section 2:

$$\dot{Q}_{fins} = \dot{Q}_{pc} - \dot{Q}_{base} \quad (2)$$

$$\text{with} \begin{cases} \dot{Q}_{pc} = \dot{Q}_{tot} - \dot{Q}_{casing} & (3) \\ \dot{Q}_{casing} = \dfrac{T_{evap,max} - T_{air}}{R_{casing}} & (4) \\ \dot{Q}_{base} = \dfrac{T_{sat} - T_{air}}{R_{base}} & (5) \end{cases}$$

The casing resistance R_{casing} is evaluated experimentally with various air velocities as the global resistance for the empty vapor chamber with polymer condenser. For $1 < u_{air} \leq 3.6\ m/s$, R_{casing} can be calculated with an uncertainty of 0.1 W/K using the correlation given in equation (6) based on regression of experimental data, where R_{casing} is in K/W and u_{air} in m/s.

$$R_{casing} = [0.757\ (u_{air})^{0.325}]^{-1} \quad (6)$$

Since the air velocity is close to 3.5 m/s for all the considered experiments, R_{casing} is around 0.9 K/W. This value includes convective and radiative heat transfer, as well as conduction through the casing.

The thermal resistance of the condenser base plate R_{base}, on the other hand, is estimated theoretically as the sum of a conductive and a convective resistance:

$$R_{base} = \frac{t_{base}}{\pi(r_{seal}^2 - N r_{ext}^2)\lambda_{base}} + \frac{1}{\pi(r_{seal}^2 - N r_{ext}^2)h_{conv}} \quad (7)$$

with t_{base} the thickness of the plate, λ_{base} its thermal conductivity, r_{seal} the seal inner radius, N the number of tubes of the condenser and r_{int} and r_{ext} their inner and outer radii. The convective heat transfer coefficient h_{conv} is considered equal to that measured at the fins and defined later in this section. The resulting R_{base} value is 2.0 ± 0.4 K/W for the polymer condenser and 0.9 ± 0.5 K/W for the aluminum condenser.

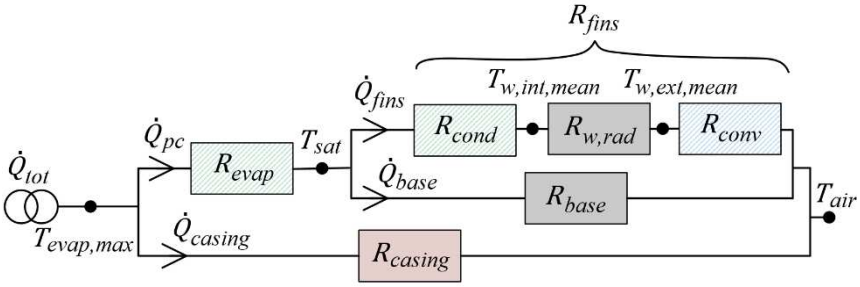

Fig. 9. Equivalent electrical network of the heat transfer in the vapor chamber

At high heat load, around 30% of $\dot{Q}_{tot}$ is transferred through the casing and the part of $\dot{Q}_{pc}$ evacuated through the polymer condenser base plate is smaller than 15%. In the end, the fins transfer 60 - 65% of the total heat load. This percentage decreases with $\dot{Q}_{tot}$. For the aluminum condenser, about 30% of the phase-change heat load is transferred through the base plate. As a result, the fins transfer at most 50% of the total heat load.

1.3.2 Thermal resistances

The thermal resistance of evaporation R_{evap} is associated with phase change in the evaporator area and depends on the liquid charge. Since the copper evaporator casing is 3 mm thick, the conductive thermal resistance is negligible. The heat transfer coefficient at the evaporator is defined on the basis of the resistive heater surface, of radius r_{heater}, as follows:

$$h_{evap} = \frac{1}{\pi (r_{heater})^2 R_{evap}} \quad \text{with} \quad R_{evap} = \frac{T_{evap,max} - T_{sat}}{\dot{Q}_{pc}} \tag{8}$$

Since NCG are supposed to affect heat transfer mainly in the fins region, the corresponding thermal resistance R_{fins} is studied in the present work:

$$R_{fins} = \frac{T_{sat} - T_{air}}{\dot{Q}_{fins}} \tag{9}$$

R_{fins} is used to investigate the NCG influence regardless of the phenomena occurring at the evaporator. As shown in Fig. 9, R_{fins} can be divided into three resistances according to the heat transfer phenomena involved:

$$R_{fins} = R_{cond} + R_{w,rad} + R_{conv} \tag{10}$$

The condensation resistance R_{cond} includes both the condensate film resistance and the interfacial resistance presented in the following section. $R_{w,rad}$ is the radial conductive resistance of the tubes wall and R_{conv} is related to forced air convection cooling outside the condenser tubes.

As mentioned previously, the external wall temperature is the mean temperature measured by IR camera. Consequently, the average convective heat transfer coefficient is estimated by:

$$h_{conv} = \frac{1}{2\pi r_{ext} N H_{tot} R_{conv}} \quad \text{with} \quad R_{conv} = \frac{T_{w,ext,mean} - T_{air}}{\dot{Q}_{fins}} \tag{11}$$

The internal wall temperature is unknown. $R_{w,rad}$ is thus calculated from the condenser tubes' properties and geometry:

$$R_{w,rad} = \frac{t_w}{2\pi r_{ln} N H_{tot} \lambda_w} \quad \text{with} \quad r_{ln} = \frac{r_{ext} - r_{int}}{ln(r_{ext}/r_{int})} \tag{12}$$

where t_w is the thickness of the tube wall and λ_w, its thermal conductivity. The conductivities of the PET and aluminum are taken equal to 0.20 W/m.K and 200 W/m.K, respectively. The condensation thermal resistance is then deduced as:

$$R_{cond} = \frac{T_{sat} - T_{w,ext,mean}}{\dot{Q}_{fins}} - R_{w,rad} \tag{13}$$

1.3.3 Uncertainty analysis

The uncertainty in $\dot{Q}_{fins}$ is calculated using the following expressions:

$$\begin{cases} \Delta\dot{Q}_{fins} = \sqrt{\left(\Delta\dot{Q}_{pc}\right)^2 + \left(\dot{Q}_{base}\right)^2 \left[\left(\frac{\Delta R_{base}}{R_{base}}\right)^2 + \frac{\Delta T_{sat}^2 + \Delta T_{air}^2}{(T_{sat} - T_{air})^2}\right]} & (14) \\ \Delta\dot{Q}_{pc} = \sqrt{\left(\Delta\dot{Q}_{tot}\right)^2 + \left(\dot{Q}_{casing}\right)^2 \left[\left(\frac{\Delta R_{casing}}{R_{casing}}\right)^2 + \frac{\Delta T_{evap,max}^2 + \Delta T_{air}^2}{(T_{evap,max} - T_{air})^2}\right]} & (15) \end{cases}$$

Given the uncertainty in the measurement of the thermocouples located in the chamber and the difference between the two sensors, a precision of ± 1.5 K is considered for the saturation temperature. The experimental uncertainties in the temperatures T_{air} and $T_{evap,max}$ are 2.5 and 0.2 K, respectively. Equation (14) yields an uncertainty between 3.5 W at low heat load and 5 W at high heat load for the polymer condenser, and between 5.5 and 10 W for the aluminum condenser.

The uncertainty in the thermal resistances and heat transfer coefficients are obtained in the same way as that of the heat load.

1.4 Vapor chamber performance

1.4.1 Comparison of polymer and aluminum condensers

In this section, the effect of NCG on the results is minimized through suitable choice of data: the vapor chamber performance is evaluated for both polymer and aluminum condensers using experimental results obtained with the initial NCG mass (i.e. the time t_{vacuum} is minimum) and sufficiently high heat loads. The liquid charge is identical in both cases and about 10 mL. It is optimized for the highest heat transfer rate and remains the same for all the data points.

Fig. 10 shows the evolutions of R_{cond}, $R_{w,rad}$ and R_{conv}, whose sum is equal to R_{fins}, with respect to the heat load transferred by the polymer (Fig. 10a) and aluminum (Fig. 10b) fins. The condensers' properties detailed previously and used for calculation have been summarized in Table 1, section 3.1. The thermal resistances decrease when $\dot{Q}_{fins}$ increases. The casing and condenser base plate resistances are also included in Fig. 10 (red and black lines). R_{casing} is the same in both cases and is two to three times higher than R_{fins}, whereas R_{base} is two times smaller for the aluminum condenser than for the polymer one. As a result, $\dot{Q}_{pc}$ is similar in both cases but a larger portion of the heat load is transferred through the aluminum plate and $\dot{Q}_{fins}$ is smaller in Fig. 10b than in Fig. 10a. The pie charts present the relative contributions of R_{cond}, $R_{w,rad}$ and R_{conv} to R_{fins} for the highest heat load. In the polymer case (Fig. 10a), the convective cooling resistance is preponderant (63%), followed by R_{cond}. The contribution of $R_{w,rad}$ is smaller than 10% despite the low thermal conductivity of polymer. The condensation resistance for the aluminum condenser has similar values as for the polymer one (Fig. 10b). The aluminum wall resistance is negligibly small, whereas the contribution of R_{conv} is over 70%. The limiting phenomenon is thus air convection cooling in both cases.

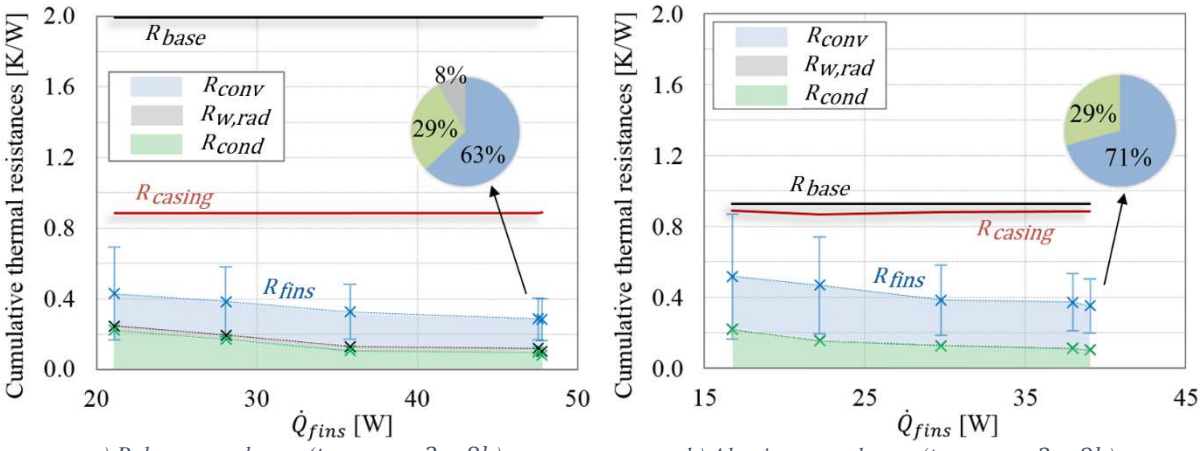

a) Polymer condenser ($t_{vacuum} = 2 - 8h$) *b) Aluminum condenser ($t_{vacuum} = 2 - 8h$)*

Fig. 10. Comparison of contributions for the thermal resistances adding up to R_{fins} and comparison with R_{casing} and R_{base}

For the polymer condenser, the convective heat transfer coefficient was consistently calculated at 85 ± 30 W/m².K from equation (11). This value is independent of the heat load. Experimental results have been compared to the empirical correlations of Grimison (1937) [32-34] and Zukauskas

(1987) [35-36,32] for arrays of cylinders in cross flow. With an air velocity of 3.5 m/s, the correlation of Grimison gives an average heat transfer coefficient of 117 W/m².K. The correlation of Zukauskas yields two different values: 107 W/m².K for aligned tubes and 111 W/m².K for staggered tubes. The coefficients seem somewhat overestimated by correlations but they are consistent with experimental results. For the aluminum condenser, experiments gave a convective heat transfer coefficient of 65 ± 25 W/m².K. The larger tube external diameter is partly the cause of the lower value of h_{conv}. Besides, the uncertainty in the air velocity is not negligible (± 18% or 0.6 m/s) and the air temperature is not homogeneous over the duct section, which might create a bias in h_{conv} since the fins height is different between the polymer and aluminum condensers.

The global thermal resistances of the polymer and aluminum condensers, presented in Fig. 11, decreases when the heat load increases, mainly because boiling develops. The heat transfer coefficient at the evaporator based on the heat source area rises with the heat load: it is between 1100 W/m².K and 1800 W/m².K. It is independent of the condenser. Besides, the global thermal resistances obtained with the polymer and aluminum condensers are equal despite a thermal resistance 250 times higher for the polymer wall and some differences in the condenser geometry. The design of the aluminum condenser leads to a reduced convective heat transfer coefficient, but this may be balanced by increased conduction through the base plate. In any case, the influence of the material thermal conductivity on the results is low since air convection cooling is the limiting phenomenon. Polymer being lightweight and cheap, it is of interest for the manufacturing of air-cooled condensers with hollow fins.

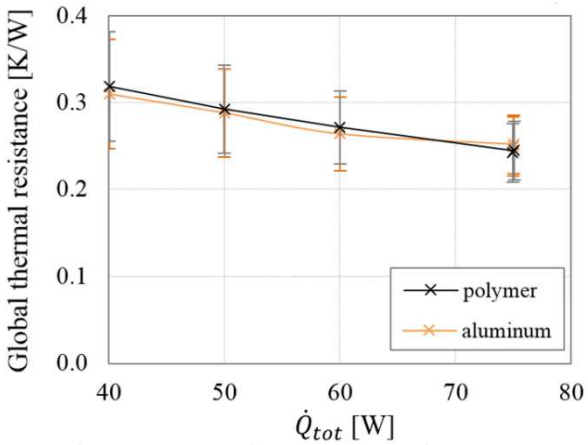

Fig. 11. Comparison of the global thermal resistances measured with the polymer and aluminum condensers

1.4.2 Impact of the presence of non-condensable gas

The presence of NCG usually impacts the performance of heat pipes because they accumulate at the condenser and deteriorate condensation heat transfer by forming a barrier to the condensing vapor at the liquid-vapor interface. In some cases, depending on the NCG quantity and operating conditions, condensation completely ceases in all or part of the condenser. In the present study, IR visualizations of the condenser are performed to determine the external temperature profile of the fins (see section 1.2). The temperature profile depends on the evolution of the heat flux along the fin, which is in turn influenced by NCG. For both polymer and aluminum condensers, experiments were conducted over one week in order to study the impact of NCG on the temperature profiles and on the vapor chamber thermal performance at high and low heat transfer rates. The fluid fill charge is almost identical in both cases and remains unchanged since the vapor chamber was not emptied between tests.

The effect of NCG on the wall temperature profiles of tubes #1 to 3 is presented in Fig. 12 for the polymer condenser and two heat inputs. The legend labels correspond to the elapsed time from the last vacuum pumping of the vapor chamber: the longer the time t_{vacuum}, the higher the NCG mass, which can be estimated in the order of a few milligrams. The temperature of the tubes are close except for a low NCG mass at low heat load (blue curves in Fig. 12a). The initial temperature differences observed between curves is mainly due to variations of the cooling air temperature. An increase in

t_{vacuum} and thus in the NCG mass $m_{nc,tot}$ causes the temperature front to shift to the bottom of the tube since a larger volume is occupied by NCG. The NCG quantity also affects $\dot{Q}_{fins}$ indirectly: the thermal resistance of the fins increases with $m_{nc,tot}$, thus reducing the part of the total heat load transferred by the fins. The temperature profile shift is then the result of both a higher NCG mass and a lower effective heat load. The two effects are difficult to dissociate experimentally. Furthermore, the front seems steeper when $m_{nc,tot}$ rises. The temperature difference between the top of the tube (where $T_{w,ext}$ is close to T_{air}) and its bottom ($T_{w,ext} \approx T_{sat}$) is also influenced by NCG: it increases with $m_{nc,tot}$ because, for a comparable heat load, the effective surface for heat transfer is smaller when the quantity of NCG is high. This mechanism explains the degradation of the condenser thermal performance caused by NCG, which is studied later in this section. The comparison of Fig. 12a and Fig. 12b shows that the height affected by NCG is greater when $\dot{Q}_{fins}$ is low.

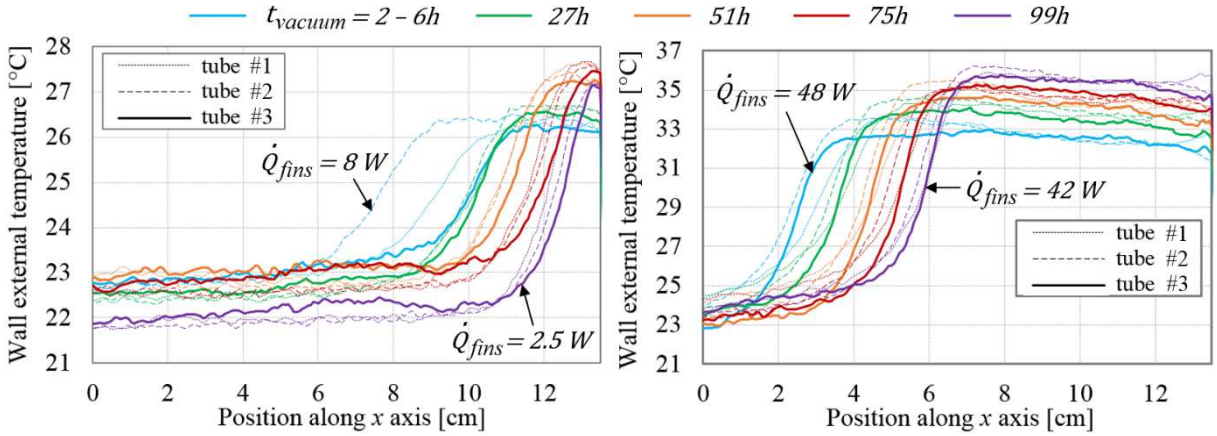

a) Low heat load ($\dot{Q}_{tot}$ = 20 W, $\dot{Q}_{fins}$ = 2.5-8 W) *b) High heat load ($\dot{Q}_{tot}$ = 75 W, $\dot{Q}_{fins}$ = 42-48 W)*

Fig. 12. Effect of NCG on external wall temperature profiles with polymer condenser ($m_{nc,tot}$ increases with t_{vacuum})

A similar study was conducted with the aluminum condenser (Fig. 13) with the same heat inputs as previously. A single profile is presented for each experiment because they are similar from one fin to another. Fig. 13 shows no significant difference between the temperature profiles. At low heat load, $\dot{Q}_{fins}$ is really small, possibly because the fins are entirely filled with NCG from the initial time.

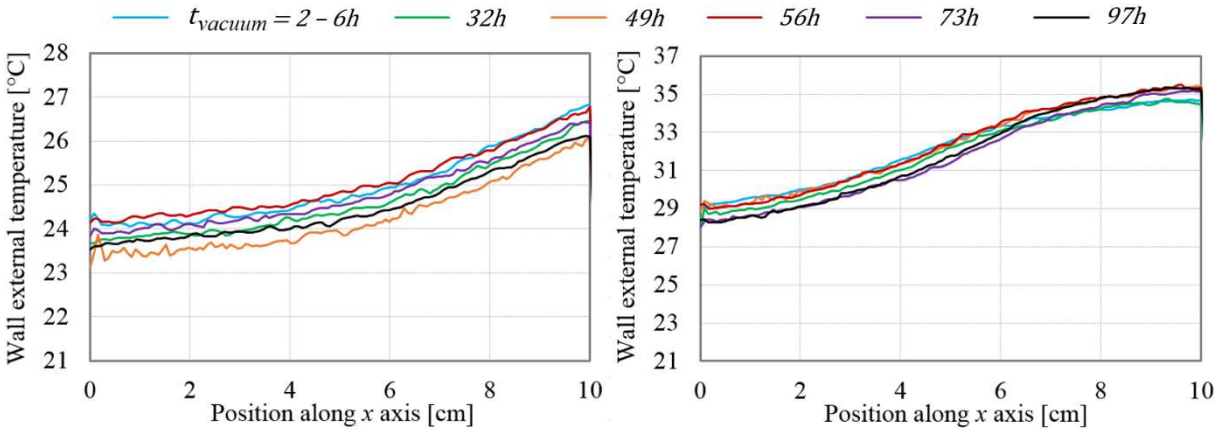

a) Low heat load ($\dot{Q}_{tot}$ = 20 W, $\dot{Q}_{fins}$ = 2-4 W) *b) High heat load ($\dot{Q}_{tot}$ = 75 W, $\dot{Q}_{fins}$ = 38-39 W)*

Fig. 13. Effect of NCG on external wall temperature profiles (tube #3) with aluminum condenser

The evolution of the global thermal resistance R_{tot} as a function of the elapsed time from vacuum pumping is presented in Fig. 14. The influence of NCG is noticeable for the polymer condenser, particularly at low heat load: between the first and last experiment, R_{tot} increases by nearly 50% for $\dot{Q}_{tot}$ = 20 W and by 20% at 75 W. The impact is not as evident for the aluminum condenser, all the more since uncertainties are large.

Since NCG are supposed to mainly affect heat transfer at the condenser, their effect on R_{fins} is shown in Fig. 15 as a function of $\dot{Q}_{fins}$. In the polymer case, it can be observed that the presence of NCG deteriorates the condenser performance: R_{fins} increases continuously with t_{vacuum}. Besides, the NCG influence is much greater on the condenser performance than on the global one and still increases when the heat load decreases: R_{fins} rises by 450% at low heat load and 45% at high heat load between $t_{vacuum} = 2 - 8h$ and $99h$. Concerning the aluminum condenser (Fig. 15b), the effect of NCG seems negligible at high heat load. At low heat load, no general trend emerges from the data and uncertainties are massive because $\dot{Q}_{fins}$ is close to zero. Therefore, no definitive conclusions can be drawn from the results.

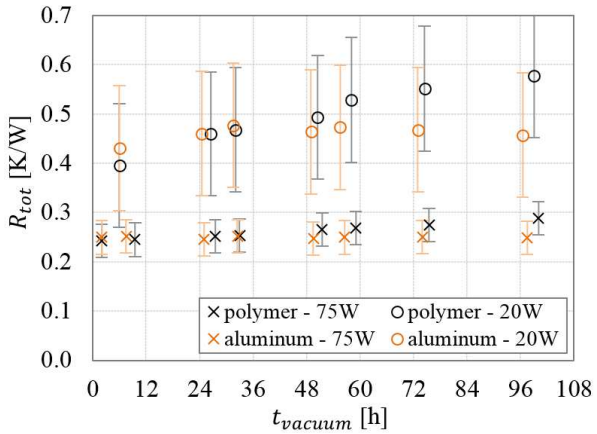

Fig. 14. Effect of NCG on global thermal resistance ($m_{nc,tot}$ increases with t_{vacuum})

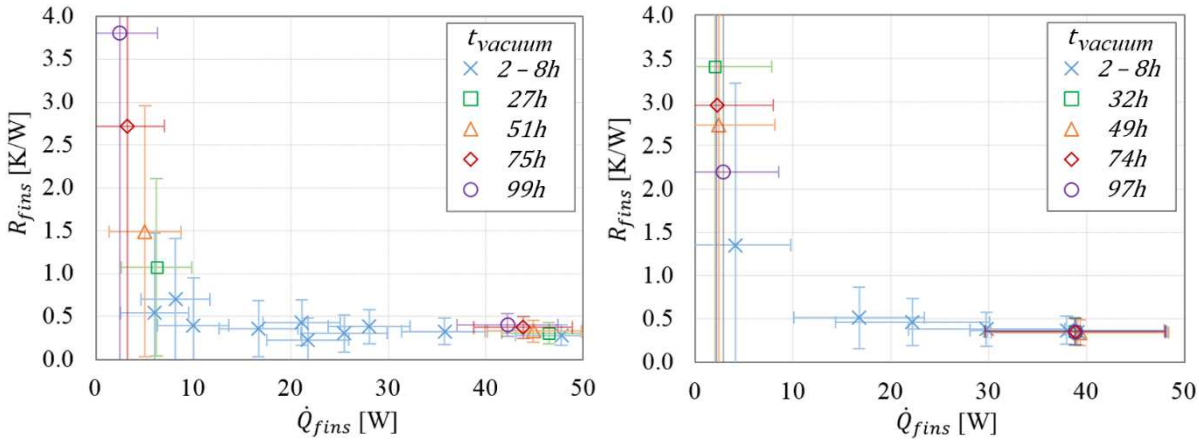

a) Polymer condenser *b) Aluminum condenser*

Fig. 15. Effect of NCG on the fins thermal resistance ($m_{nc,tot}$ increases with t_{vacuum})

1.4.3 Synthesis

The experimental study has shown that radial heat conduction through the fins wall does not influence the vapor chamber performance because air-cooling is the limiting phenomenon for heat transfer (section 1.4.1). Axial heat conduction, on the other hand, may have an impact on the results. Because of it, the height affected by NCG in the aluminum condenser is not visible from the IR temperature profiles, unlike in the polymer case. Axial conduction might also affect the distribution of NCG inside the fins. The performance degradation due to NCG is pronounced for the polymer condenser, especially at low heat load. Concerning the aluminum condenser, the impact is not discernible from the available experimental data. It might be slightly more sensitive to NCG because, unlike the polymer condenser, it seems to be entirely filled by NCG at low heat load from the initial mass.

Following experimentations, a model was developed in order to achieve a better understanding of the NCG effect in air-cooled condensers with hollow fins by knowing, for instance, the NCG distribution inside the fins, which is difficult to obtain experimentally. The impact of the NCG mass and of the effective heat transferred by the fins could also be uncoupled thanks to the model.

2. Numerical model of film condensation inside a vertical tube in the presence of non-condensable gas

As explained in the introduction, gas-loaded heat pipe models present different levels of complexity in the treatment of mass diffusion between vapor and NCG. Flat-front models completely neglect diffusion while, in 1D models, axial diffusion is taken into account. The most sophisticated models include axial and radial diffusion through 2D formulations. Some authors [11-12] tried to discern when 2D effects must be accounted for in thermosyphons. They defined dimensionless parameters to characterize the importance of these effects depending, for instance, on the tube's geometry and properties, on the working fluid, the NCG mass and on the diffusion coefficient. However, model validation from experiments and analysis were conducted for thermosyphons of diameter around 3 or 4 cm. Since the studied condensers are made of 5.3 mm inner diameter tubes, radial diffusion is considered negligible and a 1D diffuse-front approach was chosen as a satisfactory compromise between model accuracy and computation time. The developed model focuses on film condensation in the presence of NCG inside one of the condenser tubular fins. It is somewhat similar to Edwards and Marcus's work [5] on a gas-loaded capillary heat pipe. However, since the vapor chamber under study works as a thermosyphon, the present model has to account for the condensate film thickness evolution along the tube. Axial mass diffusion is considered, as well as axial and radial heat conduction in the fin wall.

The physical model consists of a tubular hollow fin of height H_{tot}, with r_{int} and r_{ext} as internal and external radii. A schematic diagram of the condenser tube, which is quite similar to Hijikata's [11] (Fig. 1), is shown in Fig. 16. The tube is closed on its top. During vapor chamber operation, the gas is swept toward the condenser section by the vapor and, since it does not condense, accumulates at the condenser end, forming a barrier to vapor flow and condensation. In some cases, depending on the NCG quantity and operating conditions, this leads to a complete shut-off of condensation in the upper part of the tube. Heat transfer is then negligible in this region, as well as the condensate film thickness δ. The vapor chamber operates at steady state with stationary NCG. A 1D hydrodynamic model coupled to Fick's diffusion equation and to a thermal model is presented here for an axisymmetric condenser hollow fin. The hydrodynamic model is similar to previous works on heat pipes [37]. The NCG mass fraction w_{nc} is maximal at $x = 0$. It decreases gradually to $w_{nc} = 0$ at $x = H_{tot}$: the vapor entering the tube is considered pure. Besides, vapor-pressure drop in the pipe is neglected, so the total pressure is uniform throughout the tube. However, the saturated vapor and NCG mixture properties vary in the x direction due to axial mass diffusion, convection and film condensation.

2.1 Hydrodynamic modelling

The tube is divided longitudinally into several control volumes, for which the balance equations are written. For the liquid and the vapor, the coupled mass and energy balance equations are:

$$\frac{d\dot{m}_l}{dx}dx = \frac{\dot{q}}{h_{lv}}dx \tag{16}$$

$$\frac{d\dot{m}_v}{dx}dx = -\frac{\dot{q}}{h_{lv}}dx \tag{17}$$

where x is the coordinate along the axis, $\dot{m}$ is the mass flow rate, $\dot{q}$ is the heat transfer rate per unit length calculated in the thermal model (section 2.3) and h_{lv} is the latent heat of vaporization of the fluid. Subscripts l and v denote the liquid and the vapor, respectively.

The momentum balance equation for the liquid derives from the formulation written by Lips *et al.* [37], who showed in conditions comparable to those of the present study that the transfer of momentum due to condensation and the interfacial shear stress were negligible:

$$\rho_l \frac{d\left(A_l u_l^2\right)}{dx} dx = -A_l \frac{dP_l}{dx} dx + \rho_l g A_l sin\theta dx - |\tau_{lw}| L_{lw} dx \tag{18}$$

P is the pressure, A is the cross section, u the velocity, ρ the density, g the gravitational acceleration, θ the inclination of the tube measured from the horizontal position, τ the shear stress and L the wetted length. Subscript w denotes the wall.

Since the total pressure is assumed uniform throughout the tube and $\theta = \pi/2$, equation (18) becomes:

$$\rho_l \frac{d\left(A_l u_l^2\right)}{dx} dx = \rho_l g A_l dx - |\tau_{lw}| L_{lw} dx \tag{19}$$

On the side of the control volume, the liquid cross section varies (Fig. 17). Introducing the liquid film thickness δ and knowing that

$$\begin{cases} u_l = \dot{m}_l / \rho_l A_l & (20) \\ A_l = \pi\delta(2r_{int} - \delta) & (21) \\ L_{lw} = 2\pi r_{int}\,, & (22) \end{cases}$$

the momentum balance equation for the liquid can be rearranged as:

$$\frac{d\delta}{dx} = \frac{\delta(2r_{int} - \delta)}{\dot{m}_l(r_{int} - \delta)} \frac{d\dot{m}_l}{dx} + \rho_l \left(\frac{\pi\delta}{\dot{m}_l}\right)^2 \frac{(2r_{int} - \delta)^2}{2(r_{int} - \delta)} [2r_{int}|\tau_{lw}| - \rho_l g\delta(2r_{int} - \delta)] \tag{23}$$

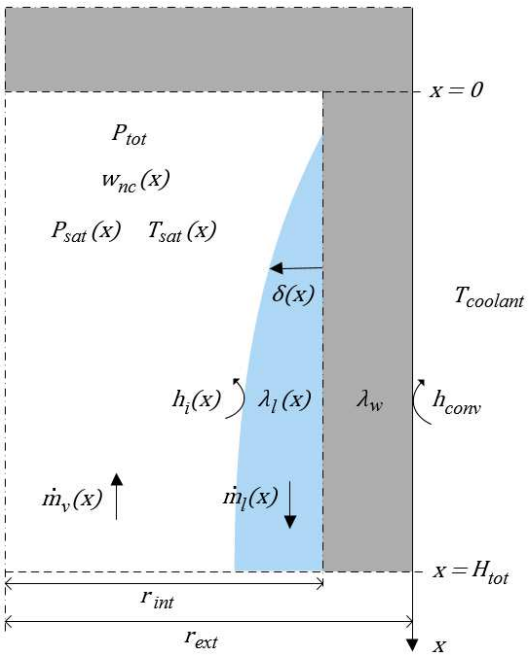

Fig. 16. Model of film condensation inside a vertical tube in the presence of NCG

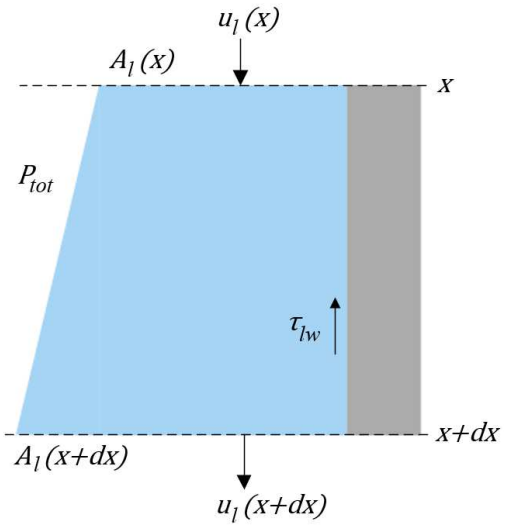

Fig. 17. Control volume in the liquid flow

For wall shear stress calculation, the liquid flow is assumed to be laminar:

$$\tau_{lw} = \frac{1}{2}\rho_l u_l^2 f \quad \text{with} \quad f = \frac{Po}{\mathcal{R}e} \tag{24}$$

where f is the friction factor, Po the Poiseuille number and $\mathcal{R}e$ the Reynolds number.

Since the interfacial shear stress is small compared to the liquid-wall shear stress, τ_{lw} is calculated assuming a free liquid-vapor interface [37]. The Poiseuille and Reynolds numbers are then determined

by considering two parallel plates of width $2\pi r_{int}$. For a fully developed flow and a plate spacing of 2δ, Shah and London [38] give

$$f\mathcal{R}e = 24 \tag{25}$$

and the Reynolds number can be expressed as follows:

$$\mathcal{R}e = \frac{\rho_l u_l D_h}{\mu_l} \quad \text{with} \quad D_h = \frac{4\pi r_{int}\delta}{\pi r_{int} + \delta} \tag{26}$$

where D_h is the hydraulic diameter and μ is the dynamic viscosity.
Considering $r_{int} \gg \delta$, equation (26) reduces to:

$$\mathcal{R}e = \frac{4\rho_l u_l \delta}{\mu_l} \tag{27}$$

Combining equations (24), (25) and (27), the liquid-wall shear stress becomes:

$$\tau_{lw} = \frac{3u_l\mu_l}{\delta} \tag{28}$$

2.2 Non-condensable gas diffusion modelling

Application of Fick's law of diffusion to the NCG mass flow, accounting for both convection and mass diffusion, yields [29]:

$$\dot{m}_{nc} = w_{nc}(\dot{m}_v + \dot{m}_{nc}) - \rho_g A_v \mathcal{D}\frac{dw_{nc}}{dx} \tag{29}$$

where w is the mass fraction and $\mathcal{D}$ is the diffusion coefficient for NCG in vapor. Subscripts nc and g stand for the non-condensable gas and the gas mixture (vapor and NCG), respectively. The vapor cross section can be expressed as:

$$A_v = \pi(r_{int} - \delta)^2 \tag{30}$$

Since NCG is assumed stationary, $\dot{m}_{nc} = 0$ and equation (29) can be written as:

$$\frac{dw_{nc}}{dx} = \frac{w_{nc}\dot{m}_v}{\rho_g \pi (r_{int} - \delta)^2\, \mathcal{D}} \tag{31}$$

The NCG mass fraction is defined as follows:

$$w_{nc} = \frac{\rho_{nc}}{\rho_v + \rho_{nc}} \tag{32}$$

Gas phase diffusion coefficients depend on the particle size and molecular mass of the considered species, but it is also a function of pressure and temperature. Tang *et al.* [39] have compiled and evaluated the gas phase diffusion coefficients of many compounds, including n-pentane and ethanol in air at 298 K. They give pressure-independent diffusion coefficients (also called diffusivity) of which the SI derived unit is Pa.m².s^{-1} and hereby noted $\mathcal{D}_P$. The diffusion coefficient $\mathcal{D}$ in equation (31) includes the pressure and temperature effects through the following relationship [39]:

$$\mathcal{D} = \frac{\mathcal{D}_P(T_{ref})}{P_{tot}} . \left(\frac{T_{sat}}{T_{ref}}\right)^{1,75} \tag{33}$$

where T_{ref} and T_{sat} are the diffusion coefficient reference temperature and the saturated vapor temperature, respectively. The binary diffusion coefficients reported by Tang *et al.* [39] have been measured for trace gases in the atmosphere, conditions that are different from the case studied here. However, diffusion coefficient data is sparse in the literature and this study is the only one we found that closely matched our needs. According to Tang *et al.*, $\mathcal{D}$ is a function of the bath gas pressure: the latter was approximated by the total pressure P_{tot}, sum of the vapor and NCG partial pressures, in equation (33).

Considering NCG as ideal gas, the mixture density appearing in equation (31) is given by:

$$\rho_g = \rho_v + \rho_{nc} = \rho_v + \frac{\bar{M}_{nc}(P_{tot} - P_v)}{\bar{R}\, T_{sat}} \tag{34}$$

where $\bar{M}$ is the molar mass and $\bar{R}$ the ideal gas constant. In each control volume, NCG and vapor are assumed to be at the same temperature T_{sat}, the vapor saturation temperature at pressure P_v. The vapor pressure is a function of the NCG mass fraction w_{nc} and is calculated at every axial position with the following relationship:

$$P_v = \frac{\bar{M}_{nc}(1 - w_{nc})}{\bar{M}_{nc}(1 - w_{nc}) + \bar{M}_v w_{nc}} P_{tot} \tag{35}$$

2.3 Thermal modelling

In the thermal model, as in the hydrodynamic model, the tube is axially divided into several control volumes of height dx (Fig. 18). Conduction in the wall is modeled by two constant thermal resistances: $R_{w,ax}$ in the axial direction and $R_{w,rad}$ in the radial direction. At the top and bottom ends of the tube, axial conduction through the cylindrical sleeve of the cap (R_{top}) and condenser base plate (R_{bottom}) is considered. As for forced air convection cooling outside the tube, the heat transfer coefficient between the fin external wall and the cooling air flow h_{conv} is assumed constant and independent of the wall temperature. The air temperature $T_{coolant}$ is also constant.

Inside the tube, phase change at the liquid-vapor interface and conduction through the condensate film must be taken into account. Two local thermal resistances R_i and R_f are thus defined, at each node j along the x axis:

$$\begin{cases} R_i^j = \dfrac{1}{2\pi(r_{int} - \delta^j) dx h_i^j} & (36) \\ R_f^j = \dfrac{1}{2\pi r_{int} dx h_f^j} \quad \text{with} \quad h_f^j = \dfrac{\lambda_l^j}{\delta^j} & (37) \end{cases}$$

Subscripts i and f denote the liquid-vapor interface and the condensate film, respectively. Longitudinal conduction in the film is neglected, as well as heat conduction through the gas phase. The axial evolutions of the film thickness δ and of the saturated vapor pressure and temperature, from which the liquid properties depend, are given by the coupled hydrodynamic and NCG diffusion models described previously. The iterative resolution procedure is detailed in section 2.4.

At the liquid-vapor interface, the heat transfer coefficient h_i is derived from the gas kinetic theory [40]:

$$h_i^j = \frac{2a_c}{2 - a_c} \frac{\rho_v^j (h_{lv}^j)^2}{T_{sat}^j} \frac{1}{\sqrt{2\pi \dfrac{\bar{R}}{\bar{M}_v} T_{sat}^j}} \left(1 - \frac{P_v^j}{2\rho_v^j h_{lv}^j}\right) \tag{38}$$

where a_c is the accommodation coefficient. As mentioned in [37], this coefficient is very difficult to determine experimentally and thus not well referenced in the literature. Furthermore, the coefficient h_i given in equation (38) does not take into account the NCG effect on condensation as it accumulates at the liquid-vapor interface. A large amount of research has been performed about condensation in the presence of NCG and reviewed by Huang *et al.* in 2015 [41]. Several heat transfer correlations are available in the literature: some are empirical and others semi-theoretical. Semi-theoretical correlations are based on the heat and mass transfer analogy. They are more versatile than empirical formulas but usually require an iterative resolution. The influence of the heat transfer coefficient h_i calculated using these models is studied in the appendix, showing that radial diffusion has a negligible impact on the temperature profiles compared to axial diffusion in the case studied.

The energy balance in each control volume leads to a set of equations as follows:

$$\begin{cases} \dfrac{T_{sat}^1 - T_w^1}{R_i^1 + R_f^1 + R_{w,rad}} + \dfrac{T_w^2 - T_w^1}{R_{w,ax}} = \dfrac{T_w^1 - T_{coolant}}{R_{w,rad} + R_{conv}} + \dfrac{T_w^1 - T_{coolant}}{R_{top} + R'_{conv}} & \text{for } x = 0 \quad (39) \\ \dfrac{T_{sat}^j - T_w^j}{R_i^j + R_f^j + R_{w,rad}} + \dfrac{T_w^{j+1} - T_w^j}{R_{w,ax}} = \dfrac{T_w^j - T_{coolant}}{R_{w,rad} + R_{conv}} + \dfrac{T_w^j - T_w^{j-1}}{R_{w,ax}} & \text{for } 0 < x < H_{tot} \quad (40) \\ \dfrac{T_{sat}^n - T_w^n}{R_i^n + R_f^n + R_{w,rad}} + \dfrac{T_{sat}^n - T_w^n}{R_{bottom}} = \dfrac{T_w^n - T_{coolant}}{R_{w,rad} + R_{conv}} + \dfrac{T_w^n - T_w^{n-1}}{R_{w,ax}} & \text{for } x = H_{tot} \quad (41) \end{cases}$$

The equations are solved for the n unknown wall temperatures using a tridiagonal matrix algorithm, also known as Thomas algorithm. The saturation temperature profile is determined from the vapor partial pressure given by the NCG diffusion model (section 2.2, equation 35).

The thermal model is used to calculate the heat transfer rate per unit length, which is a parameter of the hydrodynamic model:

$$\dot{q}^j = \frac{\dot{Q}^j}{dx} = \frac{T_{sat}^j - T_w^j}{\left(R_i^j + R_f^j + R_{w,rad}\right) dx} \quad (42)$$

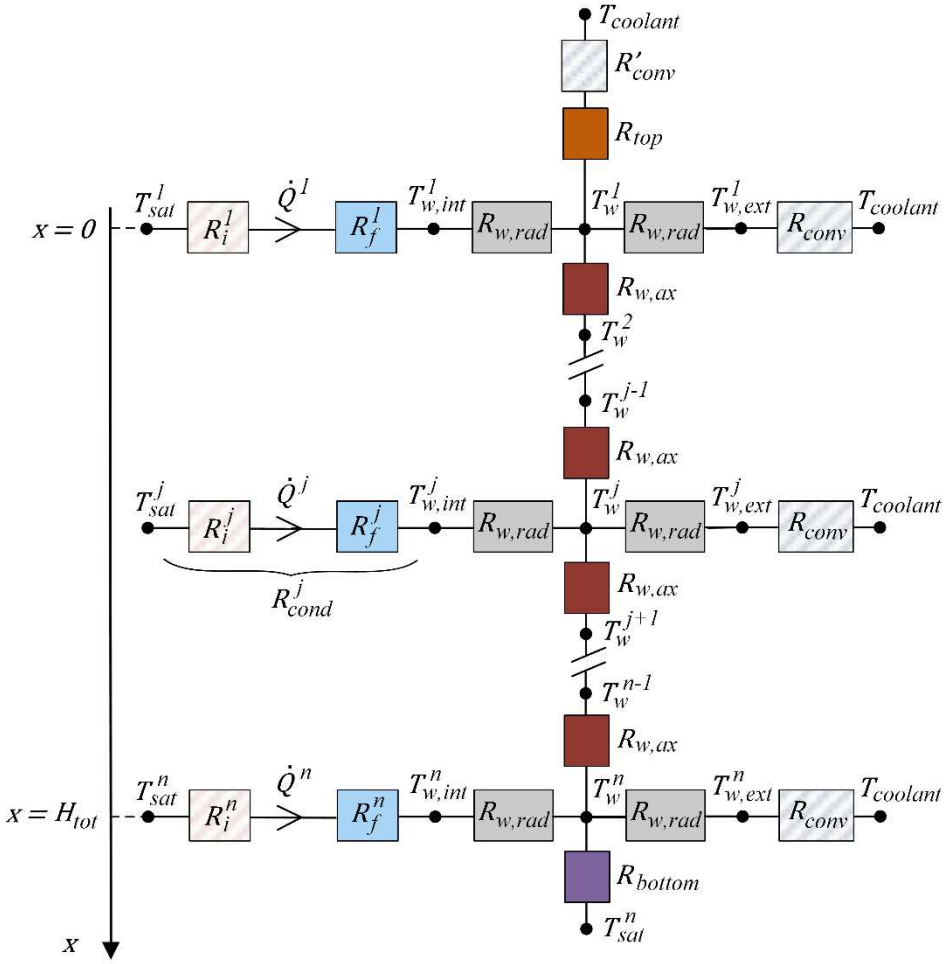

Fig. 18. Thermal nodal network diagram

2.4 Resolution procedure

The iterative resolution procedure of the coupled hydrodynamic, diffusion and thermal models as implemented into MATLAB is presented in Fig. 19. The condenser geometry (number of tubes N, height and radius of tubes) is given as input data, as well as the conductivity of the wall material λ_w. The air convection cooling parameters $T_{coolant}$ and h_{conv} and the operating conditions of the vapor

chamber (fluid, total heat transferred by the fins $\dot{Q}_{fins}$) are also specified. Lastly, the input data include the total NCG mass present in the condenser $m_{nc,tot}$, its molar mass $\bar{M}_{nc}$ and the diffusivity $\mathcal{D}_P$ of NCG in vapor (or, symmetrically, of vapor in NCG).

1 - The first step in the resolution procedure is initialization, which is shown in blue dashed lines in Fig. 19. For the initialization, axial heat conduction in the wall is neglected.

1 - a) Starting from a guess value of the NCG mass fraction at the top w_{nc}^1 and of the saturation temperature T_{sat}^n at the tube entrance, the total pressure and the boundary conditions of the hydrodynamic and NCG diffusion models are determined. The total pressure is assumed equal to the pure saturated vapor pressure at T_{sat}^n or, in other words, there is no NCG at the tube entrance ($w_{nc} = 0$ at $x = H_{tot}$). Since the saturation temperature cannot be smaller than $T_{coolant}$, w_{nc} has a maximum value evaluated from reversed equation (35):

$$w_{nc,max} = \frac{\bar{M}_{nc}(P_{tot} - P_{sat}(T_{coolant}))}{\bar{M}_{nc}(P_{tot} - P_{sat}(T_{coolant})) + \bar{M}_v P_{sat}(T_{coolant})} \tag{43}$$

The remaining boundary conditions at $x = 0$ are given as follows:

$$\begin{cases} \delta = \delta_0 & (44) \\ \dot{m}_l = \pi\delta(2r_{int} - \delta)\,\rho_l u_l \quad \text{with} \quad u_l = \dfrac{g\rho_l\delta^2}{3\mu_l} & (45) \\ \dot{m}_v = 0 & (46) \end{cases}$$

A sensitivity study showed that the results are independent of the initial film thickness δ_0, which is taken to be 10^{-7} m. The expression of u_l in equation (45) comes from the momentum balance equation for the liquid, equation (23), considering $d\delta/dx = d\dot{m}_l/dx = 0$ and $r_{int} \gg \delta$. The velocity u_l was not taken as zero because the matrix to solve would then be close to singular but, as for δ, its initial value is negligible compared to the obtained values when x increases.

1 - b) The coupled hydrodynamic and diffusion models, consisting of four ordinary differential equations, are solved using *ode23s* MATLAB solver with the aforementioned boundary conditions. Several closure equations are needed to express the liquid-wall shear stress, the diffusion coefficient and the mixture density (see Fig. 19). The heat transfer rate per unit length is calculated from equation (47) neglecting axial heat conduction in the wall:

$$\dot{q}^j = \frac{T_{sat}^j - T_{coolant}}{\left(R_i^j + R_f^j + 2R_{w,rad} + R_{conv}\right)dx} \tag{47}$$

The saturation temperature and the vapor and liquid properties used in the model, namely ρ_v, h_{lv}, ρ_l, μ_l and λ_l, come from the NIST database REFPROP. They are calculated for each control volume through polynomial regressions implemented into MATLAB and relating them to the vapor partial pressure or temperature.

1 - c) The resulting heat transfer rate is calculated as follows:

$$\dot{Q}_{fins,out} = N.\sum_{x=0}^{H_{tot}} \dot{q}^j\,dx \tag{48}$$

The temperature T_{sat}^n is adjusted iteratively and steps *1-a* to *1-c* are repeated until $\dot{Q}_{fins,out}$ matches the input heat load.

1 - d) The total NCG mass is computed as:

$$m_{nc,tot,out} = N.\sum_{x=0}^{H_{tot}} dm_{nc}^j \quad \text{with} \quad dm_{nc}^j = \pi(r_{int} - \delta^j)^2\,\frac{\bar{M}_{nc}(P_{tot} - P_v^j)}{\bar{R}T_{sat}^j}\,dx \tag{49}$$

The initial mass fraction w_{nc}^1 is updated and steps *1-a* to *1-d* are repeated until the convergence criterion on the total NCG mass is satisfied.

2 - Thanks to the output data of the hydrodynamic and diffusion models, the thermal model can be solved to find the wall temperatures accounting for axial heat conduction in the wall. Once again, the temperature T_{sat}^{n} is adjusted iteratively to obtain the desired heat load, which is now an output of the thermal model.

3 - Once the thermal model has been solved, the hydrodynamic and NCG diffusion models have to be run again. The boundary conditions are still determined as explained in step *1-a*, with T_{sat}^{n} coming from the thermal model. Furthermore, the heat transfer rate per unit length is calculated from the wall temperatures with equation (42).

4 - Steps 2 and 3 are repeated until the convergence criterion on the NCG mass fraction profile is satisfied. The parameters of the problem being tightly coupled, an under-relaxation coefficient is sometimes needed on w_{nc}^{j} to keep the computation stable.

5 - The resulting NCG mass is calculated from equation (49) and, if it does not match the given value, w_{nc}^{1} is updated and steps 2 to 4 are repeated. Since w_{nc} has a maximum value, adjusting the initial mass fraction might be impossible in some cases. The whole profile is then shifted to the bottom or to the top of the tube before solving the thermal model again, according to the difference between the obtained and desired values of $m_{nc,tot}$. For instance, when the value of w_{nc}^{1} is maximum because the saturation temperature equals $T_{coolant}$ at $x = 0$, an additional mass increase shifts the NCG front to the bottom of the tube. The iterative resolution ends when the convergence criteria on the heat load, on the NCG mass fraction profile and on the total NCG mass are reached simultaneously.

The model enables to calculate the condensate film thickness, the vapor and liquid mass flow rates and the NCG mass fraction along the tube for a given heat load and NCG mass, as well as the saturation and wall temperature profiles. The calculation time depends on the importance of axial heat conduction in the wall compared to the other modes of heat transfer. The model has been run on a standard PC. The setup configuration for the machine is: Intel Core i5-4590 (3.30 GHz), 4 GB RAM, 227 GB HDD, OS Windows 7 Pro and MATLAB R2015a 8.5. Axial heat conduction is neglected for the initialization, which generally requires a few minutes depending on the suitability of the initial guess for w_{nc}^{1} and T_{sat}^{n}. For a polymer tube, it takes only a few additional seconds to solve the final model because axial conduction has a low impact on the results. For an aluminum tube, on the other hand, solving the final model may require several tens of minutes because the wall thermal conductivity has a substantial influence and must be gradually increased. However, when the model has been solved with aluminum once, it is possible to save time by choosing appropriate initialization data and varying only the heat load or the NCG mass.

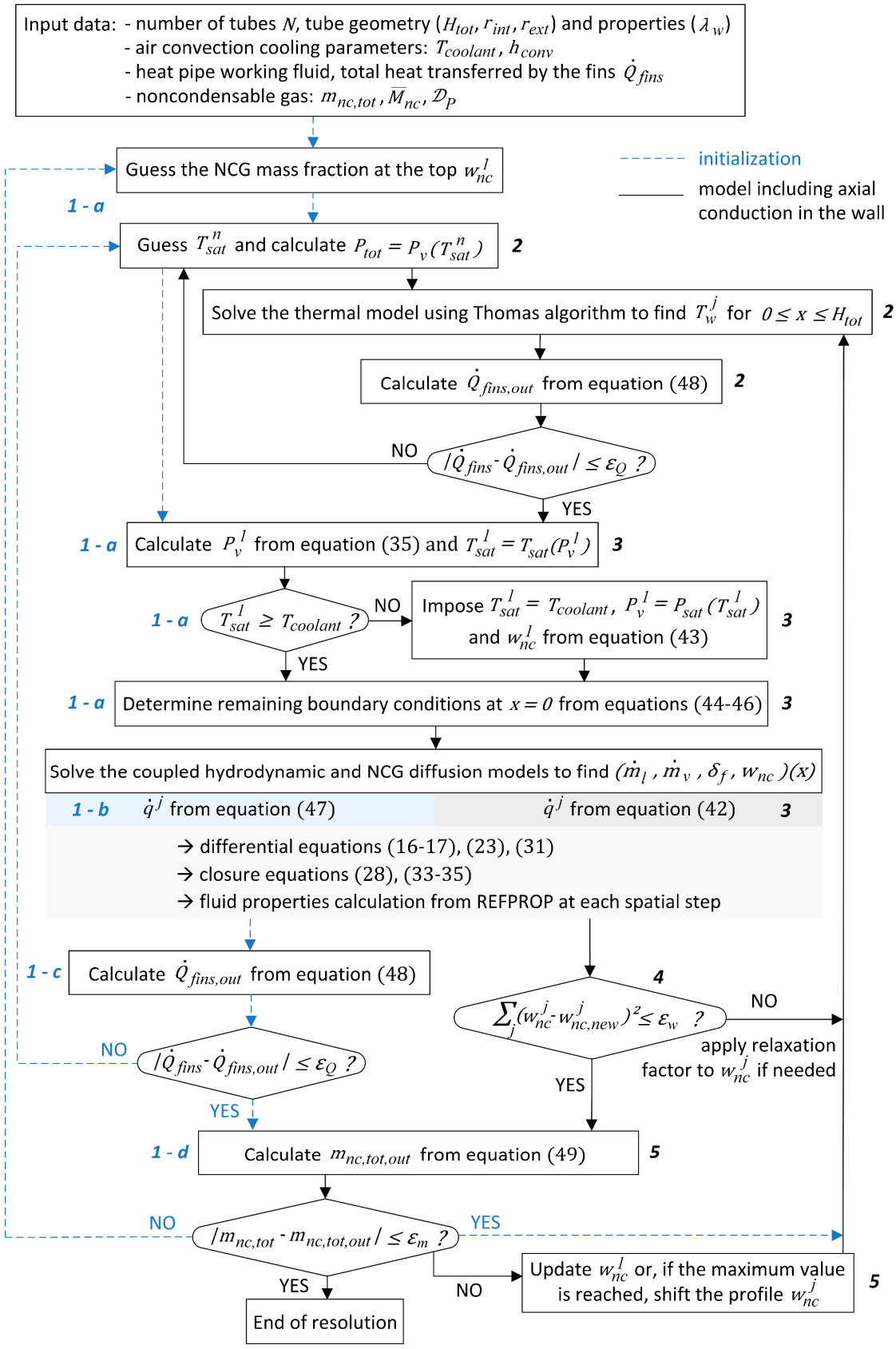

Fig. 19. Iterative resolution procedure of the coupled hydrodynamic, diffusion and thermal models

3. Modelling results and discussion

3.1 Comparison of model predictions with experiments

Model predictions are compared with the experimental results obtained with the polymer and aluminum condensers. Input parameters for the simulation of experimental conditions are summarized in Table 1. The modeled geometry corresponds to the actual system for each case (see section 1.1 for the experimental setup description). For each data point, the model was solved with input parameters $\dot{Q}_{fins}$, h_{conv} and T_{air} matching the measured values.

Table 1. Input parameters of the model for comparison with experiments

Condenser tubes geometry and properties			Vapor chamber operating conditions		
	polymer	aluminum		polymer	aluminum
number of tubes N	27		working fluid	n-pentane	
H_{tot} [mm]	135	100	non-condensable gas	air	
r_{int} [mm]	2.65		$\mathcal{D}_P$ [Pa.m².s^{-1} at 298 K]	0.87 [39]	
t_w [mm]	0.3	1.0	$\dot{Q}_{fins}$ [W]	2 – 50	2 – 40
λ_w [W.m^{-1}.K^{-1}]	0.2	200	h_{conv} [W.m^{-2}.K^{-1}]	85	65
t_{top} [mm]	10	1	$T_{coolant}$ [°C]	21 – 24	
t_{base} [mm]	5				

The comparison of the measured external wall temperature profiles for the polymer condenser (colored lines) with profiles obtained from the model (black dashed lines) is presented in Fig. 20. Since the experimental NCG mass is unknown due to degassing phenomena, the input value of $m_{nc,tot}$ was adjusted in the model so that a good agreement between predicted and experimental data at a given heat input $\dot{Q}_{fins}$ is reached. The discrepancies, observed especially at high heat load, could be explained by the non-homogeneity of the air temperature over the fins during experiments and by the variation of surface emissivity.

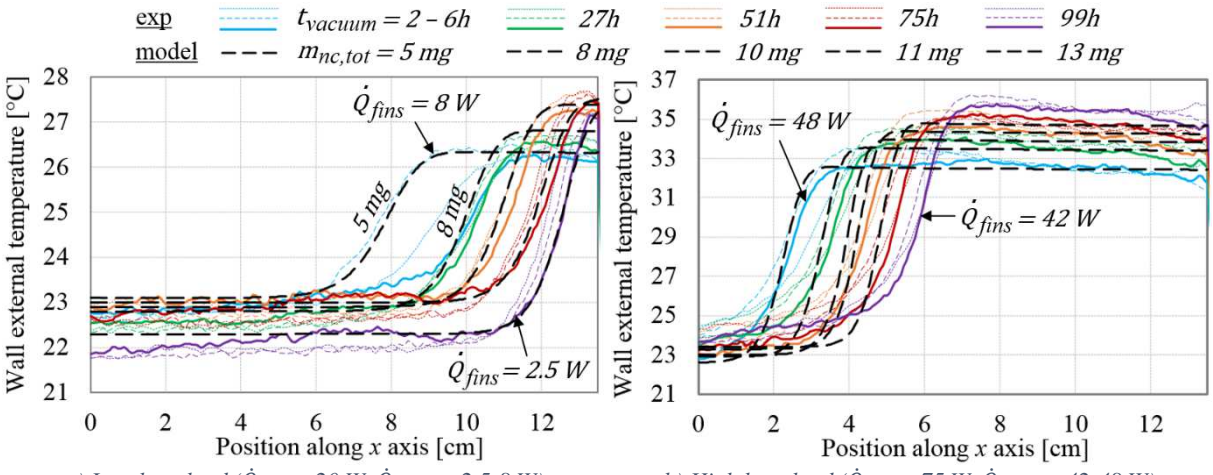

a) Low heat load ($\dot{Q}_{tot}$ = 20 W, $\dot{Q}_{fins}$ = 2.5-8 W) *b) High heat load ($\dot{Q}_{tot}$ = 75 W, $\dot{Q}_{fins}$ = 42-48 W)*

Fig. 20. Comparison of model predictions with experimental results for the polymer condenser

For the aluminum condenser, the comparison between experimental and modelling results is shown in Fig. 21. It is presented at high heat load only because the model is not applicable to cases where NCG occupy the whole height of the tube, which happens at really low heat loads. The model indeed assumes that there is no NCG at the tube entrance. Like for the polymer condenser, the

agreement between the measured temperature profiles and those exported from the model is quite good when adjusting the input NCG masses.

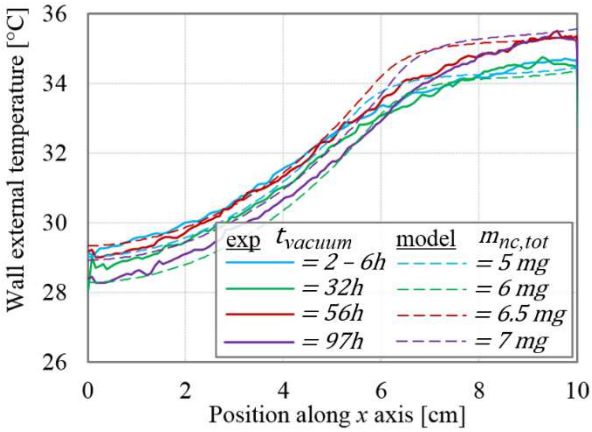

Fig. 21. Comparison of model predictions with measured wall temperature profiles for the aluminum condenser at high heat load ($\dot{Q}_{tot}$ = 75 W, $\dot{Q}_{fins}$ = 38-39 W)

3.2 Parametric study

A parametric study is conducted in order to evaluate the sensitivity of the model to uncertain parameters. Another objective is the comparison of polymer and aluminum condensers of strictly identical geometry.

3.2.1 Influence of uncertain input parameters of the model on the wall temperature profile

Among the input parameters, the NCG mass is not the only one being difficult to estimate: the uncertainties in $\dot{Q}_{fins}$ and h_{conv} derived from experiments are significant. Their effect on the wall temperature profile is thus studied for the polymer condenser at low and high heat loads in Fig. 22. These results have to be compared with the experimental results of Fig. 12, where the effects of the heat load and of the NCG could not be dissociated. This can be done using modelling results.

Fig. 22a and Fig. 22b show that, when $m_{nc,tot}$ rises, the front is shifted to the right (i.e. to the bottom of the tube) because NCG occupies a larger volume. For a similar heat load, the effective surface for heat transfer is then reduced, leading to an increase in the temperature difference between the top and the bottom ends of the tube. This is consistent with the analysis of experimental results detailed in section 1.4.2.

The influence of the heat transferred by the fins on the temperature profile is presented in Fig. 22c and Fig. 22d. A higher heat load shifts the front to the top of the tube. Besides, an increase in $\dot{Q}_{fins}$ generates a larger temperature difference between the tube ends and a steeper front. Hence, the temperature rise observed in Fig. 12 is due to the increase in the NCG mass rather than the decrease of the heat transferred by the fins.

Lastly, the effect of a variation in h_{conv} is visible in Fig. 22e and Fig. 22f. Since air-cooling is the limiting phenomenon for heat transfer as explained in section 1.4.1, a change in h_{conv} has a significant impact on the saturation temperature and thus on the temperature at the bottom of the fin. If the convection coefficient is reduced, so is the efficiency of heat transfer. Therefore, T_{sat} and the temperature difference between the two ends of the tube increase.

From the comparison of Fig. 22 (a), (c), (e) to Fig. 22 (b), (d), (f), is can be deduced that the sensitivity of the temperature profile to the NCG mass is more pronounced at low heat loads whereas at high heat loads, it is more affected by the heat dissipated by the fins and by the external convective heat transfer coefficient.

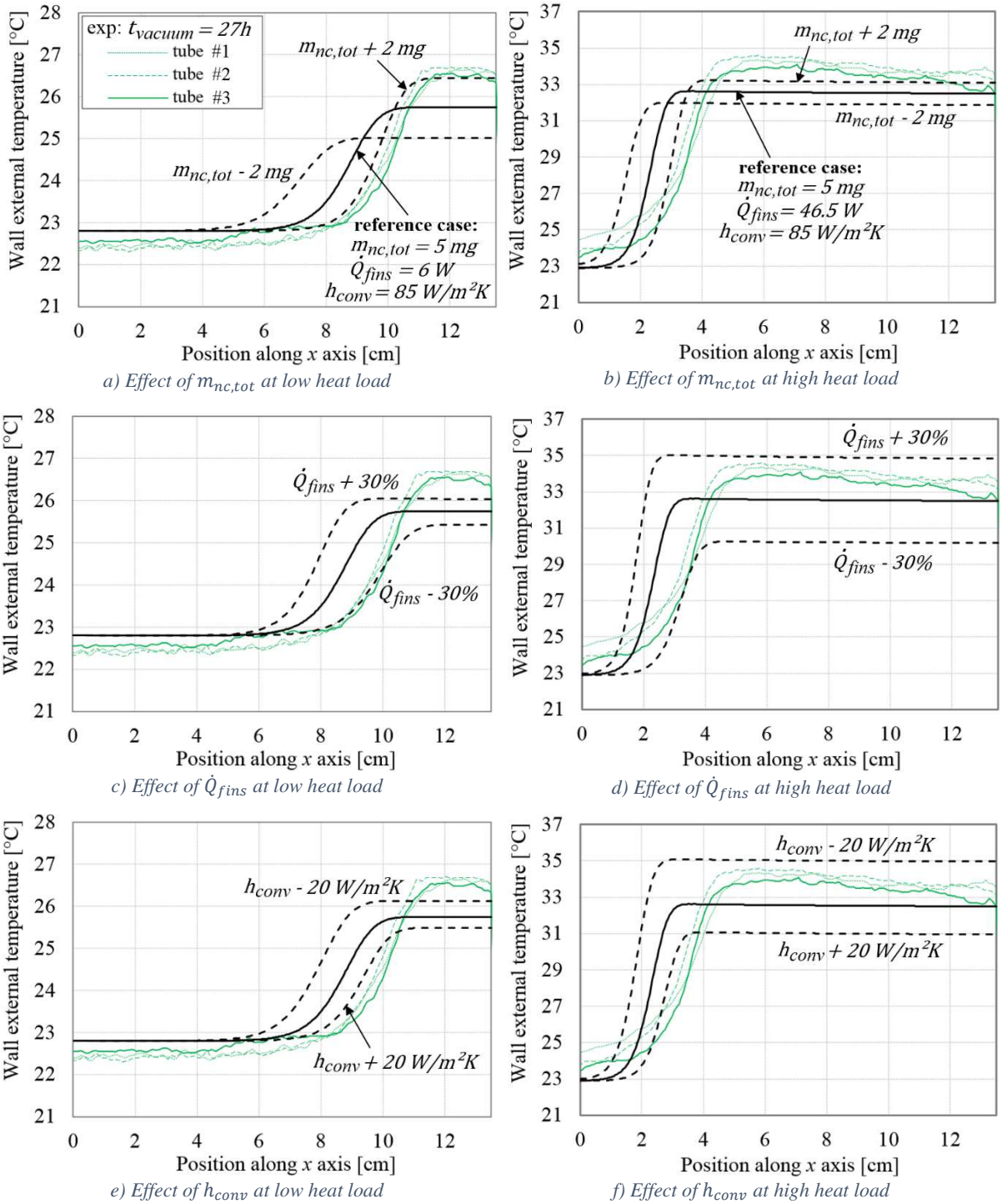

a) Effect of $m_{nc,tot}$ at low heat load

b) Effect of $m_{nc,tot}$ at high heat load

c) Effect of $\dot{Q}_{fins}$ at low heat load

d) Effect of $\dot{Q}_{fins}$ at high heat load

e) Effect of h_{conv} at low heat load

f) Effect of h_{conv} at high heat load

Fig. 22. Effect of input parameters $m_{nc,tot}$, $\dot{Q}_{fins}$ and h_{conv} on the wall temperature profile with the polymer condenser

3.2.2 Influence of wall thermal conductivity on the temperature profiles

Thanks to the numerical model, polymer and aluminum condensers can be compared considering the exact same geometry (the reference being the polymer condenser geometry given in Table 1) and identical operating conditions. The only varying parameter is then λ_w, which is a thousand times higher for aluminum (λ_w = 200 W/m.K) than for polymer (λ_w = 0.2 W/m.K). The external cooling coefficient h_{conv} was set at 100 W/m².K and the coolant temperature at 23°C. The model was solved in both cases for $\dot{Q}_{fins}$ = 75 W and $m_{nc,tot}$ = 5 mg. The results are presented in Fig. 23.

The saturation and external wall temperature profiles are displayed in Fig. 23a. The wall temperatures for polymer and aluminum condensers are relatively close because air-cooling is the limiting phenomenon in both cases. The difference that is observed at the top of the tube is due to longitudinal heat conduction in the wall. Longitudinal conduction is indeed negligible for polymer but not for aluminum. It tends to smooth the temperature profiles, leading to higher temperatures at the top of the tube. Concerning the saturation temperature, it is higher in the polymer case because of a significantly greater wall thermal resistance in the radial direction compared to aluminum. The saturation temperature at the bottom of the tube T_{sat}^{n} is used in the thermal resistance calculation:

$$R_{fins} = \frac{T_{sat}^{n} - T_{air}}{\dot{Q}_{fins}} \tag{50}$$

According to the model, the performance of an air-cooled aluminum condenser is better than that of an air-cooled polymer condenser of same geometry: the increase in R_{fins} when using polymer instead of aluminum is around 15% at 75 W. This percentage decreases slightly when $m_{nc,tot}$ rises because the polymer condenser is somewhat less affected by NCG than the aluminum one: the presence of 5 mg of NCG leads to a 13% increase in R_{fins} compared to pure vapor in the former case and a 15% increase in the latter case.

The higher sensitivity of the aluminum condenser to NCG can be explained using Fig. 23b, which presents the NCG mass fraction profiles. The mass fraction w_{nc} indirectly depends on the saturation temperature through equation (35): it decreases when T_{sat} increases. Since the wall and saturation temperatures at the top of the tube are higher for aluminum because of longitudinal heat conduction, NCG mass fractions are lower and the volume occupied inside the aluminum fins is greater compared to polymer fins. Consequently, the wall conductivity influences the gas distribution, which in turn affects the condenser's sensitivity to NCG.

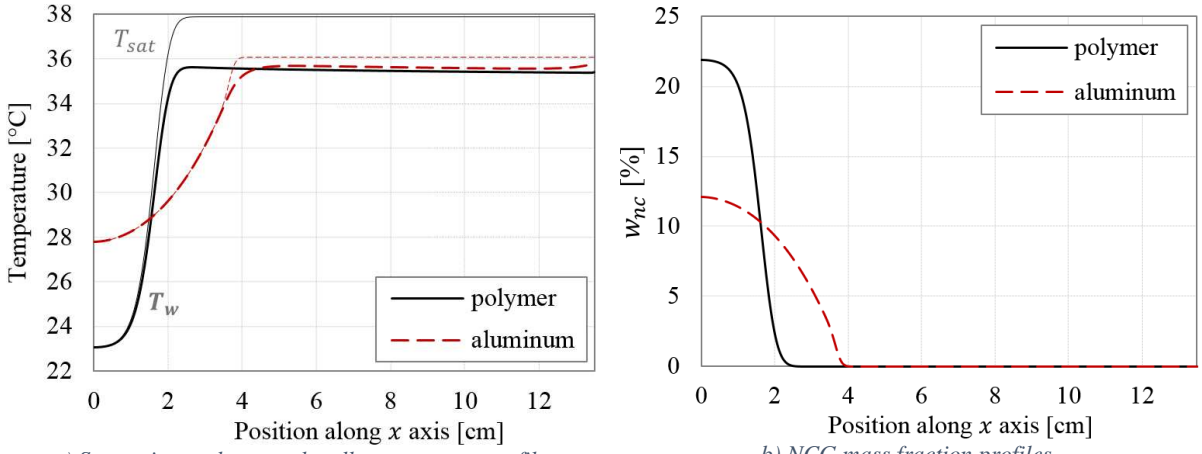

a) Saturation and external wall temperature profiles

b) NCG mass fraction profiles

Fig. 23. Comparison of modelling results between polymer and aluminum fins for $\dot{Q}_{fins} = 75$ W and $m_{nc,tot} = 5$ mg

Overall, the difference between air-cooled aluminum and polymer condensers is relatively small regarding the absolute performance as well as the degradation due to NCG. However, the effect of the wall conductivity strongly depends on the operating conditions. Additional simulations considering water-cooling ($h_{conv} = 2000$ W/m².K) instead of air-cooling showed that the effect of the material on the results is all the more important as external cooling is efficient. In the absence of NCG, the impact of using polymer instead of aluminum on the thermal resistance is around ten times greater for water-cooled condensers (+200% in R_{fins} at 75 W) than for air-cooled ones. Besides, the sensitivity to NCG of water-cooled condensers is significantly affected by the choice of material: for instance, the presence of 1 mg of NCG leads to a 16% increase in R_{fins} for a water-cooled polymer condenser and a 50% increase in a water-cooled aluminum one at 75 W. By comparison, in the same

conditions, the air-cooled polymer and aluminum condensers are both marginally affected by NCG: their thermal resistance increases by 2.5% and 3%, respectively.

Conclusions

A vapor chamber with hollow fins was designed and manufactured. Experiments were carried out both with a polymer condenser and an aluminum condenser cooled by forced air convection. Air-cooling was shown to be the limiting phenomenon for heat transfer in both cases, so the performance of the condensers is almost similar. Consequently, the use of polymer is of interest for weight reduction when the cooling medium is air. The impact of NCG was studied using IR temperature measurements on the fins and performance monitoring over time. For the polymer condenser, the height affected by NCG is discernible from the IR temperature profiles and is greater at low heat loads. The performance degradation due to NCG is thus more pronounced at low heat loads, which is confirmed by the evolution of the thermal resistance. For the aluminum condenser, on the other hand, the height affected by NCG is not visible due to axial heat conduction in the fins wall. Besides, the influence of NCG in this case is not discernible from the available experimental data.

Following experimentations, a numerical model of film condensation inside a vertical tube in the presence of NCG was developed to achieve a better understanding of the NCG effect in air-cooled condensers with hollow fins. The model combines both hydrodynamic and axial mass diffusion phenomena with 2D heat conduction in the wall. First, model predictions were compared with experimental results: a good agreement was found between the numerical model and the measured external wall temperature profiles both for the polymer and aluminum condensers, using the input NCG mass as a fitting parameter. Several other input parameters derived from experiments such as the heat load $\dot{Q}_{fins}$ or the external cooling coefficient h_{conv} influence the modelling results. Their effect on the temperature profiles was studied though a parametric analysis, as well as that of the wall thermal conductivity. The latter was shown to impact the condenser performance, which is obviously better for high conductivity materials, but also the volume occupied by NCG inside the fins. For a given set of operating conditions, when the wall thermal conductivity increases, so does the occupied volume and the impact of NCG on the thermal resistance. In other words, aluminum condensers are more sensitive to NCG than polymer ones, and the difference is all the more important as external cooling is efficient.

Even if some challenging technical aspects remain, polymer hollow-finned condensers are of interest for applications requiring weight reduction such as transportation systems, especially when the cooling medium is air. Indeed, the substitution of a metallic condenser by a polymer one having identical performance would lead to fuel economy. Concerning tightness requirements, which are generally critical for the design and manufacturing of heat pipes, they could be reduced when considering polymer condensers for a given application. Further, the use of polymer and additive manufacturing methods allow fast prototyping and a great flexibility in the shape, orientation and location of the fins. The optimization of hollow-finned condensers offers interesting prospects for future work.

Acknowledgments

We thank the members of the Industrial Technical Center for Plastics and Composites in France (IPC), especially Stéphane Garabédian and Julien Bajolet, for the manufacturing of the aluminum condenser.
This work was supported by the Carnot Institute Ingénierie@Lyon in the frame of the CAPIT4L project.

Appendix. Influence of radial diffusion on the temperature profiles

As the gas kinetic theory (equation 38) does not take radial diffusion of NCG into account, the semi-theoretical correlation proposed by No and Park [42] was tested to include this phenomenon in the calculation of h_i (which thereby depends on the NCG mass fraction). This correlation is based on the heat and mass transfer analogy but, unlike most formulations, it does not require an iterative resolution. The heat transfer coefficient is also strongly dependent on the interfacial shear stress so, according to No and Park, it is important to adopt the appropriate interfacial friction factor. In the present work, the friction factor used by Liao *et al.* [43] for counter-current flow was chosen. Besides, since the correlation is suitable for a limited range of NCG mass fractions w_{nc}, the considered h_i is:

$$h_i = \min\left(h_{i_{No\&Park}} \; ; \; h_{i_{eq(38)}}\right) \tag{A.1}$$

The comparison of h_i calculated from the gas kinetic theory and No and Park's correlation is presented in Fig. A.1 for the high heat load reference case of Fig. 22. When considering NCG, the heat transfer coefficient is greatly reduced at the top of the tube where the gas accumulates. The condensation coefficient is also shown in Fig. A.1 (bold lines). h_{cond} includes heat transfer at the liquid-vapor interface as well as through the condensate film. It is locally defined by the following equation:

$$R^j_{cond} = \frac{1}{2\pi r_{int} dx h^j_{cond}} \quad \text{with} \quad R^j_{cond} = R^j_i + R^j_f \tag{A.2}$$

When radial diffusion is not taken into account, heat conduction through the film is the limiting phenomenon all along the tube since h_{cond} is lower than h_i. With No and Park's [42] correlation, on the other hand, two regions exist: vapor condensation is limited by radial diffusion through NCG at the top of the tube (h_i smaller than h_{cond}) and by the liquid film when h_{cond} is smaller than h_i.

The effect of radial diffusion on the interface coefficient is substantial at the top of the tube. However, according to Fig. A.2, the impact of this parameter on the results seems negligible. The saturation and wall temperature profiles are indeed unchanged whatever the correlation. Since the difference between T_{sat} and T_w is really small at the top of the tube, the h_i value has no significant influence on the heat transfer in this area. In other words, in the case studied, the presence of NCG is detrimental to condensation mainly because of the induced saturation temperature reduction, and not because of a gas barrier to the condensing vapor. That is why radial diffusion has a negligible impact on the results compared to axial diffusion. The same conclusions can be drawn for the aluminum case.

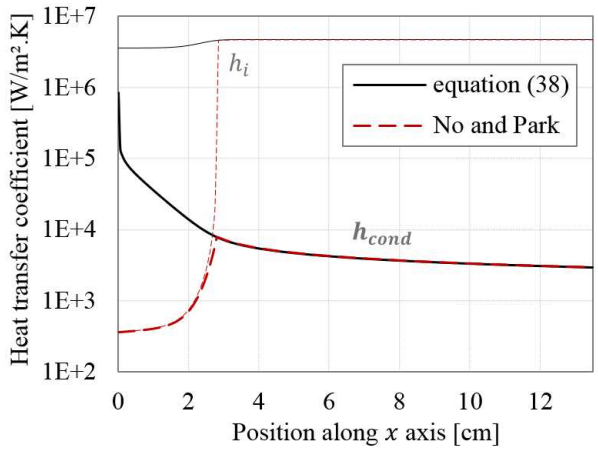

Fig. A.1. Comparison of the interface coefficient h_i calculated from equation (38) and from No and Park's [42] correlation and the resulting h_{cond} at high heat load ($m_{nc,tot} = 5\ mg$, $\dot{Q}_{fins} = 46.5\ W$, $h_{conv} = 85\ W/m^2.K$)

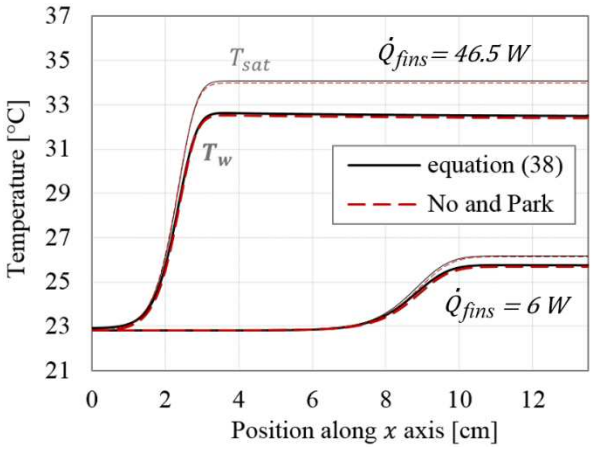

Fig. A.2. Effect of the interface coefficient h_i on the temperature profiles at high and low heat load ($m_{nc,tot} = 5\ mg$, $h_{conv} = 85\ W/m^2.K$)

References

[1] Ogata S, Sukegawa E, Kimura T. Lifetime evaluation of ultra-thin polymer pulsating heat pipe. *IEEE CPMT Symposium Japan 2014*, Kyoto, Japan (2014) 15-18.

[2] Jung C, Lim J, Kim SJ. Fabrication and evaluation of a high-performance flexible pulsating heat pipe hermetically sealed with metal. *International Journal of Heat and Mass Transfer* **149** (2020) 119180.

[3] Marcus BD, Fleischman GL. Steady state and transient performance of hot reservoir gas controlled heat pipes. *ASME* Paper No. 70-HT/SPT-11 (1970).

[4] Faghri A, Harley C. Transient lumped heat pipe analyses. *Heat Recovery Systems and CHP* **14** (1994) 351-363.

[5] Edwards DK, Marcus BD. Heat and mass transfer in the vicinity of the vapor-gas front in a gas-loaded heat pipe. *Journal of Heat Transfer* **94** (1972) 155-162.

[6] Sun KH, Tien CL. Thermal performance characteristics of heat pipes. *International Journal of Heat and Mass Transfer* **18** (1975) 363-380.

[7] Shukla KN. Transient response of a gas-controlled heat pipe. *AIAA Journal* **19** (1981) 1063-1070.

[8] Harley C. Transient analyses of noncondensible-gas-buffered two-phase heat transfer devices. *Master's thesis*, Wright State University (1993).

[9] Rohani AR, Tien CL. Steady two-dimensional heat and mass transfer in the vapor-gas region of a gas loaded heat pipe. *Journal of Heat Transfer* **95** (1973) 377-382.

[10] Harley C, Faghri A. Transient two-dimensional gas-loaded heat pipe analysis. *Journal of Heat Transfer* **116** (1994) 716-723.

[11] Hijikata K, Chen SJ, Tien CL. Non-condensable gas effect on condensation in a two-phase closed thermosyphon. *International Journal of Heat and Mass Transfer* **27** (1984) 1319-1325.

[12] Peterson PF, Tien CL. Numerical and analytical solutions for two-dimensional gas distribution in gas-loaded heat pipes. *Journal of Heat Transfer* **111** (1989) 598-604.

[13] Zhou X, Collins RE. Condensation in a gas-loaded thermosyphon. *International Journal of Heat and Mass Transfer* **38** (1995) 1605-1617.

[14] Harley C, Faghri A. Transient gas-loaded thermosyphon analysis. *Proceedings of the 10th International Heat Transfer Conference*, Brighton, UK (1994).

[15] Anderson W, Ellis M, Hartenstine J, Peters C, Tarau C, Walker K. Variable conductance heat pipes for variable thermal links. *42nd International Conference on Environmental Systems*, San Diego, California, USA (2012).

[16] Tarau C, Schwendeman C, Anderson W, Cornell PA. Variable conductance heat pipe cooling of Stirling convertor and general purpose heat source. *11th International Energy Conversion Engineering Conference*, San Jose, California, USA (2013).

[17] Lee K-L, Kadambi JR, Kamotani Y. The influence of non-condensable gas on an integral planar heat pipe radiators for space applications. *International Journal of Heat and Mass Transfer* **110** (2017) 496-505.

[18] Leriche M, Harmand S, Lippert M, Desmet B. An experimental and analytical study of a variable conductance heat pipe: Application to vehicle thermal management. *Applied thermal engineering* **38** (2012) 48-57.

[19] Huang J, Wang L, Shen J, Liu C. Effect of non-condensable gas on the start-up of a gravity loop thermosyphon with gas–liquid separator. *Experimental Thermal and Fluid Science* **72** (2016) 161-170.

[20] He J, Miao J, Bai L, Lin G, Zhang H, Wen D. Effect of non-condensable gas on the startup of a loop heat pipe. *Applied Thermal Engineering* **111** (2017) 1507-1516.

[21] Zhang JX, Wang L. Effect of air on condensation in a non-vacuum gravity heat pipe. *Applied Thermal Engineering* **114** (2017) 255-263.

[22] Cao J, Pei G, Bottarelli M, Chen C, Jiao D, Li J. Effect of non-condensable gas on the behaviours of a controllable loop thermosyphon under active control. *Applied Thermal Engineering* **146** (2019) 288-294.

[23] Wang H, Lin G, Shen X, Bai L, Wen D. Effect of evaporator tilt on a loop heat pipe with non-condensable gas. *International Journal of Heat and Mass Transfer* **128** (2019) 1072-1080.

[24] Anand AR. Investigations on effect of noncondensable gas in a loop heat pipe with flat evaporator on deprime. *International Journal of Heat and Mass Transfer* **143** (2019) 118531.

[25] Wang H, Lin G, Shen X, Bai L, Yang R, Wen D. Effect of evaporator/condenser elevations on a loop heat pipe with non-condensable gas. *Applied Thermal Engineering* **180** (2020) 115711.

[26] Kim YH, Shin DH, Kim J, Lee JH. Effect of the non-condensable gas contents on heat transfer characteristics of two-phase closed thermosyphon. *16th International Heat Transfer Conference*, Beijing, China (2018).

[27] Yuan J, Wang C, Zhang J, Ling J, Zhou Z, Gao F. Effect of non-condensable gas on thermal characteristics in two-phase closed thermosyphon. *Applied Thermal Engineering* **173** (2020) 115233.

[28] Peterson PF, Tien CL. A miniature wet-bulb technique for measuring gas concentrations in condensing or evaporating systems. *Experimental Heat Transfer* **1** (1987) 1-15.

[29] Faghri A. Heat pipe science and technology. 2nd Edition. *Global Digital Press* (2016) 1013 p.

[30] *Polymer Data Handbook*. Mark JE, Ed. Oxford University press: New York (1999) 1018 p.

[31] Cros S. Propriétés barrières des polymères utilisés en emballage. *Techniques de l'Ingénieur*, AM3160 (2007).

[32] Incropera FP, DeWitt DP. Fundamentals of Heat and Mass Transfer. 5th Edition. New York, *John Wiley & Sons* (2002), 981 p.

[33] Grimison ED. Correlation and utilization of new data on flow resistance and heat transfer for cross flow of gases over tube banks. *Trans. ASME* **59** (1937) 583-594.

[34] Kays WM, Lo RK. Basic heat transfer and flow function design data for gas flow normal to banks of staggered tubes. In: *Technical Report No. 15.* Dept. Mech Eng, Stanford University (1952).

[35] Bejan A. Convection Heat Transfer. 4th Edition. *John Wiley & Sons* (2013), 658 p.

[36] Zukauskas AA. Convective heat transfer in cross flow. In: Kakac S, Shah RK, Aung W. Handbook of Single-Phase Convective Heat Transfer. New York, *Wiley* (1987), Chapter 6.

[37] Lips S, Lefevre F, Bonjour J. Physical mechanisms involved in grooved flat heat pipes: Experimental and numerical analyses. *International Journal of Thermal Sciences* **50** (2011) 1243-1252.

[38] Shah RK, London AL. Laminar Flow Forced Convection Heat Transfer and Flow Friction in Straight and Curved Ducts - A Summary of Analytical Solutions. *Technical report*, Stanford University (1971) 308 p.

[39] Tang MJ, Shiraiwa M, Pöschl U, Cox RA, Kalberer M. Compilation and evaluation of gas phase diffusion coefficients of reactive trace gases in the atmosphere: Volume 2. Diffusivities of organic compounds, pressure-normalised mean free paths, and average Knudsen numbers for gas uptake calculations. *Atmospheric Chemistry and Physics* **15** (2015) 5585-5598.

[40] Carrey VP. Liquide-vapour phase change phenomena: an introduction to the thermophysics of vaporization and condensation process in heat transfer equipment. Bristol, *Taylor & Francis* (1992) 645 p.

[41] Huang J, Zhang J, Wang L. Review of vapor condensation heat and mass transfer in the presence of non-condensable gaz. *Applied Thermal Engineering* **89** (2015) 469-484.

[42] No HC, Park HS. Non-iterative condensation modeling for steam condensation with non-condensable gas in a vertical tube. *International Journal of Heat and Mass Transfer* **45** (2002) 845-854.

[43] Liao Y, Guentay S, Suckow D, Dehbi A. Reflux condensation of flowing vapor and non-condensable gases counter-current to laminar liquid film in a vertical tube. *Nuclear Engineering and Design* **239** (2009) 2409-2416.

Nomenclature

A	cross section, m^2
a_c	accommodation coefficient
$\mathcal{D}$	diffusion coefficient, $m^2.s^{-1}$
$\mathcal{D}_P$	diffusivity, *equation (33)*, $Pa.m^2.s^{-1}$
D_h	hydraulic diameter, m
f	friction coefficient
g	gravitational acceleration, $m.s^{-2}$
H	height, m
h	heat transfer coefficient, $W.m^{-2}.K^{-1}$
h_{lv}	latent heat of vaporization, $J.kg^{-1}$
L	length, m
m	mass, kg
$\dot{m}$	mass flow rate, $kg.s^{-1}$

$\bar{M}$	molar mass, $kg.mol^{-1}$
N	number of tubes
P	pressure, Pa
Po	Poiseuille number
$\dot{q}$	heat transfer rate per unit length, $W.m^{-1}$
$\dot{Q}$	heat transfer rate, W
r	radius or radial coordinate, m
R, R'	thermal resistance, $K.W^{-1}$
$\bar{R}$	ideal gas constant, $J.mol^{-1}.K^{-1}$
$\mathcal{R}e$	Reynolds number
t	time, s
$\mathscr{t}$	thickness, m
T	temperature, K
T_{ref}	reference temperature, *equation (33)*, K
t_{vacuum}	elapsed time from the last vacuum pumping, s
u	velocity, $m.s^{-1}$
V	volume, m^3
w	mass fraction
x	axial coordinate, m

Subscripts and superscripts

0	boundary condition at $x = 0$
air	cooling air
ax	axial
$base$	condenser base plate
$bottom$	bottom end of the tube included in the base plate
$cond$	condensation
$conv$	convection
$coolant$	external coolant fluid
$evap$	evaporator
ext	external
f	liquid film
$fins$	condenser hollow fins
g	gas mixture (vapor and NCG)
$heater$	resistive heat source
i	interface
ini	initial
int	internal
j	node number
l	liquid
max	maximum
$mean$	mean value
min	minimum
n	number of nodes
nc	noncondensable gas
out	output parameter
pc	phase change
rad	radial
sat	saturation

$seal$	sealing ring
top	top cap of the tube
tot	total
v	vapor
w	wall

Greek symbols

δ	liquid film thickness, m
Δ	difference or uncertainty
ε_m	convergence criterion on the total NCG mass, *Fig. 19*, kg
ε_Q	convergence criterion on the heat transfer rate, *Fig. 19*, W
ε_w	convergence criterion on the NCG mass fraction profile, *Fig. 19*
θ	slope of the condenser tubes, rad
λ	thermal conductivity, $W.m^{-1}.K^{-1}$
μ	dynamic viscosity, $Pa.s$
ρ	density, $kg.m^{-3}$
τ	shear stress, $N.m^{-2}$